The Function of *Efhd1*$^{+}$ Telocytes in the Synovial Lymphatic System and Inflammatory-Erosive Arthritis

Running Title: Telocyte Function in the Synovial Lymphatic System

Yue Peng[1,2], H. Mark Kenney[1,2], Sean Lydon[2], Karen L. de Mesy Bentley[1,2], Lianping Xing[1,2], Benjamin D. Korman[1,3]

Christopher T. Ritchlin[1,3] & Edward M. Schwarz[1,2*]

[1]Center for Musculoskeletal Research; [2]Department of Pathology & Laboratory Medicine; [3]Department of Medicine, Division of Allergy, Immunology, Rheumatology; University of Rochester Medical Center

*Corresponding Author; Edward_Schwarz@URMC.Rochester.edu; (585) 276-5609; University of Rochester Medical Center, 601 Elmwood Ave, Box 665, Rochester, NY, 14642, USA.

Funding: F30AG076326, T32GM007356, R01AG059775, R01AR069000, R01AR056702, and P30AR069655

Conflict of interest: No conflicts of interest to disclose.

Keywords: Telocyte, Mast Cell, Lymphatic Vessel, Electron Microscopy, Inflammatory-Erosive Arthritis, Animal Models

Telocyte Function in the Synovial Lymphatic System

Abstract (247 Words of 250)

Resting collecting lymphatic vessels (cLVs) sense edema in distal joints and initiate contractions via unknown mechanisms. Rheumatoid arthritis (RA) patients have lymphatic drainage deficiencies from affected joints, and defects in the synovial lymphatic system exacerbate inflammatory-erosive arthritis in animal models. To understand this, we generated *Efhd1*-CreER^{T2} and *Myoc*-CreER^{T2} mice for cell-specific genetic gain and loss of function studies. These mice were crossed with tdTomato reporter (Ai9) mice, and studies showed selective tamoxifen-induced transgene expression in CD31^{-}/CD34^{+} telocyte-like cells in knee and ankle synovium, and in networks physically associated with mast cells proximal to popliteal lymphatic vessels (PLVs). Consistent with the known loss of CD31^{-}/CD34^{+} telocyte in RA synovium, these cells were also decreased in TNF-tg knees and partially recovered by anti-TNF treatment. Ultrastructural and gene expression studies confirmed a distinct telocyte phenotype versus closely related fibroblasts. *In vivo* depletion studies in tamoxifen-treated *Efhd1*-CreER^{T2} and *Myoc*-CreER^{T2} mice crossed to diphtheria toxin alpha-floxed (DTA^{flox}) mice demonstrated telocyte requirements for physiologic lymphatic drainage and resolution of joint inflammation and focal erosions from zymosan-induced arthritis in the knee. *In vitro* studies demonstrated increased sensitivity to osmotic shock and decreased motility versus fibroblasts, and telocyte potential to differentiate into myofibroblasts on stiff matrix. Collectively, these findings support a model of joint homeostasis in which osmotic pressure-sensing telocyte networks extend from the synovium into mast cells proximal to joint-draining cLVs, and telocyte loss is associated with defects in the synovial lymphatic system and increased susceptibility to joint inflammation and structural damage from arthritis.

Telocyte Function in the Synovial Lymphatic System

45 **Teaser**

46 This study discovered a unique cell type (telocytes) responsible for draining inflammation from
47 arthritic joints.

48

INTRODUCTION

The lymphatic system reabsorbs excess interstitial fluid and protein for return to the central veins, and dysfunction is associated with lymphedema in affected tissues, exacerbation of chronic inflammatory diseases, and fibrosis (*1*). While some lymph migrates passively through unidirectional bicuspid lymphatic vessel valves secondary to interstitial fluid pressure and passive compression by adjacent tissue movement (*2*), the majority of lymph is transported by the contractile activity of collecting lymphatic vessels (cLVs) (*3*). Central to cLV functions are tightly regulated contraction frequency changes (*4*), known as 'pressure-induced lymphatic chronotropy' (*5*), which range from ~3 to 20 contractions/min as intraluminal pressure increases from 0.5 to 10 cmH_2O (*6, 7*) to enable coupled lymph transport with absorption via lymphatic capillaries (*8*). Recently, major advances have greatly enhanced our understanding of intraluminal pressure-induced lymphatic chronotropy and intrinsic cLV pacemaking by lymphatic muscle cells (LMCs) (*5, 6, 9, 10*). Interestingly, LMCs contain functional and molecular characteristics of both myocardium (cardiac muscle) and blood vessels (vascular smooth muscle), as evidenced by concomitant rapid cardiac-like phasic contractions to generate flow and smooth-muscle-like slow, long-lasting tonic contractions to regulate flow (*11*). However, several critical knowledge gaps remain including the identity of cells that sense acute edema in tissue distal to cLVs to trigger enhanced lymphatic clearance by initiating pacemaking signals in LMCs, and the mechanisms that underlie the loss of cLV contractility in lymphedema (*12*).

We previously demonstrated that in rheumatoid arthritis (RA), lymphatic dysfunction is a critical factor in joint inflammation, damage, and flare which can progress independent of autoimmunity (*13*). Evidence of synovial lymphatic system dysfunction in osteoarthritis (OA)

also exists (*14*). Studies on innate immune mechanisms identified increased expression of the lymphangiogenic factor vascular endothelial growth factor C (VEGF-C) in monocytes and osteoclasts, together with lymphangiogenesis in inflamed joints (*15*). Subsequent functional studies demonstrated that loss of VEGF-C signaling together with decreased lymphangiogenesis exacerbates inflammatory-erosive arthritis (*16*), while VEGF-C therapy ameliorates inflammatory arthritis by increasing lymphangiogenesis (*17*). Longitudinal MRI (*18, 19*), power Doppler ultrasound (PDUS) (*20*), and near-infrared (NIR) imaging of injected indocyanine green (ICG) dye (*7, 21*), identified three distinct mechanisms of lymphatic dysfunction in murine models of RA. The first is mediated by release of local vasodilators (e.g. nitric oxide) from inflammatory cells that contribute to reduced lymphatic flow (*13, 22*). Another involves accumulation and translocation of B cells into the sinuses of joint-draining lymph nodes, obstructing passive lymphatic flow (*19, 21, 23*). Finally, we observed the loss of cLV contractions during arthritic progression in the setting of chronic joint inflammation (*20*). In support of the translational relevance of these findings are data demonstrating that RA patients display similar lymphatic dysfunction, including reduced cLV contractility and lymphatic clearance compared to healthy controls (*24-26*), which is now a high priority area of research.

Mast cells are recognized as effective regulators of LMC contractility due to their anatomical proximity and ability to produce, store, and release various inflammatory and vasoactive mediators (*27*). Additionally, mast cells are positioned throughout the RA synovial sublining, where they comprise 5% or more of the expanded synovial cell population, and microanatomic clusters of mast cells are present in pannus tissue proximal to cartilage and bone erosion (*28*). Based on these findings and evidence from preclinical and clinical studies supporting pro-inflammatory and catabolic roles for mast cells in RA (*28, 29*), we investigated

95 mast cell effects on joint-draining lymphatics and inflammatory-erosive arthritis in tumor
96 necrosis factor-transgenic (TNF-tg) mice (*30*) and their wild-type (WT) littermates. We found
97 that popliteal lymphatic vessels (PLVs) are surrounded by an expanded frequency of
98 $MCT^+/MCPT1^+/MCPT4^+$ mast cells in TNF-tg mice, and the percentage of peri-PLV
99 degranulating mast cells was inversely correlated with lymphatic clearance (*31*). We also
100 identified a unique population of $MCT^+/MCPT1^-/MCPT4^-$ mast cells embedded within the PLV
101 cellular architecture, but the function of these cells remains unknown (*31*). Genetic and
102 pharmacologic mast cell loss of function experiments in TNF-tg mice demonstrated severe
103 lymphatic defects, which were associated with exacerbated inflammatory-erosive arthritis (*31*).
104 Collectively, these findings led us to surmise that while $MCT^+/MCPT1^+/MCPT4^+$ mast cells
105 have a well-established role in inflammation, particular mast cell subtypes are also required for
106 normal lymphatic function, proposed to be mediated by $MCT^+/MCPT1^-/MCPT4^-$ mast cells
107 embedded within PLVs. However, several unanswered questions remain including: i) the
108 anatomy and physiology of mast cell integration into the synovial lymphatic system, ii) the
109 mechanisms that facilitate recognition of increased joint fluid by the distal cLV, iii) the resulting
110 increased contraction frequency during the early phase of inflammation, and iv) how this
111 compensatory response is lost during chronic arthritis, remain be elucidated.

112 To address these questions, we developed conditional-inducible transgenic mice for
113 genetic gain and loss of function studies initially considered to specifically target LMCs. Single-
114 cell RNA sequencing (scRNAseq) studies identified three genes (*Efhd1, Myoc & Pla1a*) in
115 stromal cell population selectively expressed in PLVs compared to adjacent blood vessels (*32*).
116 We then generated three transgenic mouse lines in which a $CreER^{T2}$ cassette was knocked into
117 these genes, and the resulting animals were crossed to B6.Cg-$Gt(ROSA)26Sor^{tm9(CAG\text{-}tdTomato)Hze}$/J

118 (Ai9) (*33*) and B6.129P2-*Gt(ROSA)26Sor*$^{tm1(DTA)Lky}$/J (DTA) (*34*) mice for lineage tracing and
119 loss of function studies, respectively. Herein, we describe the construction of these models, and
120 the serendipitous finding of tamoxifen-inducible gene expression in peri-PLV spindle-shaped
121 cells with very long cytoplasmic extensions that were physically integrated into mast cells, while
122 there was no expression in the predicted LMC population (*32*), which has been further described
123 in more recent scRNAseq studies (*9*). We hypothesized the identified peri-PLV spindle-shaped
124 cells to be telocytes, which are unique mesenchymal cells found in most tissues and are
125 characterized by a small cell body and long, thin, cytoplasmic extensions called telopodes (*35*).
126 Of note are the various telocyte functions that include extracellular matrix (ECM) synthesis for
127 tissue structural support, cell-to-cell communication, regulation of immune responses, and
128 pacemaking of smooth muscle contractions (*36*). To confirm these characteristics supporting
129 telocyte identity and determine the function of telocytes within the synovial lymphatic system,
130 we performed various *in vivo* and *in vitro* studies of the tdTomato-positive (tdT^{+}) cells. Together,
131 we tested the hypotheses that: 1) networks of contiguous telocytes extend from ankle synovium
132 to PLVs, 2) telocytes are functionally distinct from lymphatic fibroblasts, and 3) synovial
133 telocytes differentiate into myofibroblasts when grown on stiff ECM.

134

135 **RESULTS**

136 **Generation of Novel CreER^{T2} Mouse Models for Genetic Targeting of Telocytes in the**
137 **Synovial Lymphatic System**

Telocyte Function in the Synovial Lymphatic System

138 We recently described single-cell RNA sequencing (scRNAseq) analysis of lymphatic vessels in
139 which we identified *Efhd1, Myoc,* and *Pla1a* as PLV-selective genes (*32*). Based on these
140 findings, we generated three knock-in mouse lines in which a *CreER*^{T2} cassette was inserted into
141 these genes of embryonic stem cells (Fig. 1a), and the resulting mice were crossed to Ai9
142 reporter mice to assess tamoxifen-induced in vivo gene targeting (Fig. 1b & c). *Ex vivo* whole-
143 mount immunofluorescent microscopy (WMIFM) revealed the presence of elongated tdT^{+} cells
144 that were preferentially clustered in networks around PLVs vs. blood vessels from tamoxifen-
145 treated *Efhd1*-CreER$^{+/-}$x Ai9$^{+/-}$ and *Myoc*-CreER$^{+/-}$ x Ai9$^{+/-}$ mice (Fig. 1d). Tamoxifen treatment
146 of younger mice (P10-P13) resulted in a similar pattern of PLV adventitial tdT^{+} cells, suggesting
147 that they maintain their identity from early postnatal development (Supplemental Fig. 1a-b).
148 These tdT^{+} cells were not found in tissues from tamoxifen-treated *Pla1a*-CreER$^{+/-}$ x Ai9$^{+/-}$ mice,
149 and these mice were not further analyzed (Supplemental Fig. 1b).

150 Interrogation of the PLV WMIFM revealed two distinct tdT^{+} populations of fibroblastic
151 cells that contained very long dendritic processes phenotypically consistent with telopodes (Fig.
152 2a). One population extended longitudinally along the PLV (Fig. 2b), and the other existed in
153 telocyte arrays within adipose tissue adjacent to PLVs (Fig. 2c). To gain wholistic insight on the
154 extent of tdT^{+} cell arrays along the PLV, we performed WMIFM on tissues from tamoxifen
155 treated *Efhd1*-CreER^{T2} x Ai9 mice with antibodies against αSMA and CD34 to label the vascular
156 smooth muscle and mast cells. Confocal images of soft-tissue extending from the ankle to the
157 knee containing the PLVs were reconstructed in 3D and stitched together (Figs. 2d-h). The high-
158 power images confirmed the presence of tdT^{+} cell arrays adjacent to PLVs that contained CD34^{+}
159 cells with a mast cell morphology. The low-resolution images revealed the networks of tdT^{+} cells
160 that paralleled the vessels from the ankle synovium to cLV.

Telocyte Function in the Synovial Lymphatic System

161 Previous investigations of lymphatic dysfunction revealed an enrichment of mast cells
162 around lymphatic vessels (*31*), which prompted us to examine these distinct tdT^+ cells and their
163 interactions within the peri-PLV tissue more closely. Scrutiny of transmission electron
164 microscopy (TEM) images of PLVs revealed elongated cells in tamoxifen-treated *Efhd1*-
165 $CreER^{+/-}$x $Ai9^{+/-}$ and *Myoc*-$CreER^{+/-}$ x $Ai9^{+/-}$ mice with morphological characteristics consistent
166 with the tdT^+ cells identified by WMIFM (Fig. 3a). Moreover, these cells have characteristic
167 ultrastructural features of telocytes (*35*) (i.e. spindle-shaped polygonal cells with a large single
168 nucleus and scant cytoplasm and thinly attenuated cytoplasmic extensions). These cells were
169 found to form intimate contacts with mast cells in what appears to be specialized junctional
170 structures at their plasma membrane interfaces suggesting active intercellular communication
171 (Fig. 3a). To validate these observations and better characterize the spatial relationships between
172 telocytes and mast cells, we conducted 3D immunofluorescent confocal microscopy. This
173 analysis demonstrated that mast cells form direct contacts with the two tdT^+ telocyte-like
174 populations (Fig. 3b and Supplemental Video 1). The spatial distribution and interaction patterns
175 observed through 3D confocal imaging precisely matched our WMIFM and TEM observations,
176 confirming that both mural and peri-PLV telocyte populations engage in direct cellular
177 interactions with mast cells. Taken together, these findings suggest a previously unrecognized
178 cellular partnership between telocytes and mast cells along lymphatic vessels, potentially
179 representing a novel signaling axis in cLV regulation.

180 To provide additional confirmation that the tdT^+ cells are telocytes, we reanalyzed our
181 published scRNAseq data on murine PLV-associated cells (*32*) to identify the *Pdgfrα*$^+$/*Cd34*$^+$
182 population known to contain telocytes and adventitial fibroblasts (*9*), which produced a uniform
183 manifold approximation and projection (UMAP) of these closely related populations (Fig. 4a).

Telocyte Function in the Synovial Lymphatic System

184 To characterize their transcriptome distinctions and similarities, we generated UMAPs of known
185 marker genes selectively expressed in either one cell type or both telocytes and fibroblasts. The
186 results confirmed that *Myoc, Efhd1, Pla1a, Dpp4, Pcsk6,* and *Ppp2r2b* genes (*9*) are
187 preferentially expressed in PLV-associated telocytes (Fig. 4b). The results also confirmed that: i)
188 the pan marker genes *CD34, Pdgfra,* and *Pdpn* have equivocal expression in both PLV-
189 associated telocytes and fibroblasts, ii) both cell types produce EMC gene products including
190 *Col1a1, Fn1,* and *Lama4*, and iii) *Comp, Dkk3* and *Angpt2* are specific marker genes for PLV-
191 associated fibroblasts. We also performed a cellular trajectory analysis of the scRNAseq data
192 from WT and TNF-tg PLVs using Monocle 3, which predicts that telocytes have the potential to
193 differentiate into fibroblasts (Fig. 4c top). Moreover, we found that there was a 47.7% decrease
194 in the proportion of telocytes relative to fibroblasts in TNF-tg mice relative to their WT
195 littermates (Fig. 4c bottom).

196 To elucidate synovial peri-lymphatic telocyte loss in TNF-tg mice, we performed
197 scanning electron microscopy (SEM) of PLVs and immunohistochemistry (IHC) on knee
198 synovium. SEM of WT PLVs revealed apparent telocyte cell bodies embedded within a very rich
199 ECM structure, and associated mast cells on top of this ECM (Fig. 4d). In contrast, SEM of
200 TNF-tg PLVs displayed varying degrees of degeneration from partial ECM loss and exposed
201 LMCs (Fig. 4e) to extensive ECM and LMC loss (Fig. 4f), which is consistent with their
202 contractility defects observed *ex vivo* (*25*). Consistent with the loss of $CD31^-/CD34^+$ telocytes
203 observed in RA synovium determined by IHC (*37*), we also observed a significant decrease in
204 $CD31^-/CD34^+$ telocyte-like cells in the synovium of TNF-tg mice receiving placebo treatment
205 compared to WT, and their partially recover from the TNF-tg mice receiving 6 weeks of anti-
206 TNF treatment (*26*) (Fig. 4g).

Telocyte Function in the Synovial Lymphatic System

207 To confirm that the CD31$^-$/CD34$^+$ synoviocytes are tdT$^+$ telocytes in our transgenic
208 mouse models, we performed flow cytometry, scRNAseq, and immunohistochemistry on lower
209 limb joint tissues from tamoxifen-treated *Efhd1*-CreER$^{+/-}$ x Ai9$^{+/-}$ and *Myoc*-CreER$^{+/-}$ x Ai9$^{+/-}$
210 mice (Fig. 5a). Flow cytometry of knee and ankle synoviocytes revealed consistent profiles of
211 tdT$^-$ and tdT$^+$ cells (Supplemental Fig. 2). The scRNAseq analysis of the flow sorted tdT$^+$
212 synoviocytes identified 13 distinct cell clusters classified by marker gene expression
213 (Supplemental Fig. 3a-b). To better characterize telocytes in the synovial cells population we re-
214 clustered the mesenchymal and stromal cell compartments (Supplemental Fig. 5c-e). The clusters
215 in the synovium closely resembled the telocyte and fibroblast clusters in lymphatics (Fig. 5b).
216 Specifically, only cells in the upper portion of the UMAP express *Efhd1* and *Pla1a* together with
217 the conventional non-specific telocyte markers *Cd34, Pdgfra, and Pdpn* (*37, 38*), which are
218 broadly expressed throughout the UMAP (Fig. 5b). In contrast to its selective expression in PLV-
219 associated telocytes, *Myoc* is broadly expressed in tdT$^+$ synoviocytes with other ECM genes
220 including: *Col1a1, Fn1,* and *Lama4* (Fig. 5b). Interestingly, cells in the lower portion of this
221 UMAP express markers associated with RA fibroblast-like synoviocytes (FLS) (*39, 40*) such as,
222 *Cdh11*, *Comp,* and *Dkk3* (Fig. 5b). Consistent with our observation that the *Efhd1*$^+$/*Pla1a*$^+$ tdT+
223 synoviocytes are telocytes, these cells are also negative for the endothelial marker gene
224 *CD31/PECAM1* (*41*), and the mesenchymal stromal cell marker *Cd90/Thy-1* (*42*) (Fig. 5b and
225 Supplemental Fig. 4). However, they are also negative for *FoxL1* (*43*) and *Ano1* (*44*) (Fig. 5b),
226 previously reported telocyte genes identified in gastrointestinal interstitial cells of Cajal (ICC)
227 (*35*).

228 Based on these scRNAseq results, we hypothesized the existence of tissue-specific
229 telocyte subsets and performed IHC studies on various tissues from tamoxifen-treated *Efhd1*-

230 CreER$^{+/-}$x Ai9$^{+/-}$ and *Myoc*-CreER$^{+/-}$ x Ai9$^{+/-}$ mice. The results from knee and ankle cryosections
231 confirmed that tdT^{+} synoviocytes are CD31^{-}/CD34^{+} cells with telocyte morphology and are
232 distinct from Comp^{+} FLS and CD31^{+}/CD34^{+} endothelial cells (Fig. 5c). Given that telocytes are
233 also known to express c-Kit (*35*), a critical gene for mast cells, we examined if c-Kit is also
234 required for telocyte development and survival. Thus, we also included joints from mast cell
235 deficient *Kit$^{W\text{-}sh/W\text{-}sh}$* (cKit$^{-/-}$) mice and confirmed that they have similar levels of synovial CD31^{-}
236 /CD34^{+} telocyte-like cells compared to WT mice (Supplemental Fig. 5), which affirms that
237 lymphatic disfunction in these animals (*31*) is likely due to the loss of mast cells and not loss of
238 telocytes that also express c-Kit. Additionally, we found tdT^{+} telocyte-like cells in tendon, skin
239 hair follicles, and within the ganglion cell layer of the retina, but no tdT^{+} cells were found among
240 the c-Kit^{+} ICC in intestine (Supplemental Fig. 6). Therefore, despite the absence of definitive
241 markers or functional assays to prove telocyte identity, the preponderance of our ultrastructural,
242 histologic, and gene expression data show that the *Efhd1*-CreER^{T2} and *Myoc*-CreER^{T2} mice
243 target tamoxifen-induced gene expression to telocyte subtypes in some but not all tissue types.

244 *In vivo* Depletion of Telocytes Decreases Lymphatic Function and Exacerbates 245 Inflammatory-Erosive Arthritis

246 To test the hypothesis that in vivo depletion of *Myoc* and *Efhd1* expressing telocytes in the
247 synovial lymphatic system are critical for lower limb lymphatic function in mice, we generated
248 an inducible depletion model by crossing the telocyte-specific CreER mice with DTA^{floxed} mice,
249 followed by tamoxifen treatment to induce diphtheria toxin-α *in vivo* depletion of the gene
250 targeted cells as outlined in Figure 6a. To estimate *in vivo* depletion efficiency in these models,
251 we performed WMIFM on PLVs and IHC knee joints from tamoxifen-treated double and single

252 (control) transgenic mice and assessed $CD31^-/CD34^+$ cells. WMIFM of PLVs demonstrated a
253 dramatic DTA elimination of telocytes on the vessel surface and the arrayed telocytes in the
254 adjacent adipose tissue (Fig. 6b). IHC analysis of the knees confirmed a ~60% reduction in the
255 number of $CD31^-/CD34^+$ synoviocytes (Figs. 6c-d). We repeated this experiment to assess
256 telocyte depletion effects on lymphatic drainage. Cohorts of single and double transgenic mice
257 underwent NIR-ICG imaging prior to tamoxifen treatment and 6hrs following the last tamoxifen
258 injection. We observed no tamoxifen effects on $DTA^{f/-}$ mice contrasted with a significant
259 reduction of ICG clearance in the tamoxifen-treated double transgenic mice (Figs. 6e-f). These
260 findings support our hypothesis that synovial lymphatic system telocytes regulate synovial
261 lymphatic clearance, although these results are confounded by our inability to assess systemic
262 effects and DTA deletion of non-telocytes (e.g. fibroblasts that differentiated from telocytes after
263 tamoxifen treatment).

264 To assess the effects of lymphatic dysfunction following telocyte deletion on acute joint
265 inflammation, we utilized the zymosan-induced arthritis (ZIA) model (*45*) as outlined in Figure
266 7a. Longitudinal ultrasound confirmed a 10-fold increase in synovial volume following knee
267 injection with zymosan vs. PBS controls (Fig. 7b-d). Moreover, zymosan-induced 3.2-fold
268 greater synovitis in telocyte depleted mice, and while this acute synovitis commenced resolution
269 in WT mice after 7 days (Fig. 7c), the increased synovial volume was unabated at day 14 in
270 telocyte depleted mice (Fig. 7d). Histology of the knee joints corroborated the imaging results
271 demonstrating increased pannus tissue in knees with ZIA from mice with depleted telocytes
272 (Figs. 7e-f). Remarkably, the histology also revealed resorbed cortical bone surfaces in DTA and
273 zymosan groups (Fig. 7e). To assess telocyte depletion and ZIA effects on focal erosions and
274 osteoclast numbers, we performed histomorphometry and micro-CT analyses on these femurs.

Telocyte Function in the Synovial Lymphatic System

275 The results showed increased numbers of tartrate-resistant acid phosphatase (TRAP) positive
276 osteoclasts on resorbed cortical bone surfaces in some of the femurs from zymosan treated mice
277 (Supplemental Fig. 7). Surprisingly, we also observed large numbers of osteoclasts in some
278 femurs from telocyte-depleted mice injected with PBS. Micro-CT further demonstrated that
279 acute ZIA failed to induce focal erosions in the knees of WT mice within 14 days, whereas it
280 induced extensive erosions in the patellar groove of telocyte-depleted mice at this time point
281 (Fig. 7g-h). Together with our lymphatic readouts, these data demonstrate that telocyte depletion
282 reduces lymphatic function, and upon challenge with acute inflammatory arthritis, leads to more
283 persistent inflammation, exacerbated synovitis, and rapid focal cortical bone loss.

284 **Synovial Lymphatic System Telocyte Function and Differentiation**

285 To investigate the potential functions of telocytes within the synovial lymphatic system,
286 we developed an in vitro model in which PLVs from tamoxifen treated *Efhd1*-CreER^{T2} x Ai9 and
287 *Myoc*-CreER^{T2} x Ai9 mice were cultured to generate a mixture of growing tdT^{+} telocytes and
288 non-fluorescent fibroblasts as described in Figure 8a. As telocytes could be the cells that sense
289 osmotic pressure in the joint from excess interstitial fluid, and intracellular Ca^{++} signaling by
290 telocytes has been studied (*46*), we assessed intracellular release of Ca^{++} following exposure to
291 sucrose and demonstrated that telocytes are more sensitive to osmotic shock than adjacent
292 fibroblasts (Fig. 8b), suggesting that signaling in response to hypertonic interstitial fluid may be
293 one of their physiological functions. To further demonstrate that telocytes are functionally
294 distinct from adjacent fibroblasts, we examined the ability of these primary telocyte and
295 fibroblast mixed cultures to migrate through Matrigel. The results demonstrated that while both

296 cell types have a chemotactic response to TGF-β, fibroblasts are more invasive than telocytes
297 (Fig. 8c).

298 Lastly, we tested the hypothesis that telocytes differentiate into robust ECM producing
299 fibroblasts, as predicted by our scRNA-seq trajectory analysis (Fig. 4c) and SEM of PLVs (Fig.
300 4d). These experiments utilized FACS purified cultures of tdT^+ telocytes derived from PLVs
301 harvested from tamoxifen-treated *Efhd1*-$CreER^{T2}$ x Ai9 and *Myoc*-$CreER^{T2}$ x Ai9 mice, which
302 retained their telocyte phenotype as evidenced by their long telopodes and their CD34 and Myoc
303 protein expression (Supplemental Fig. 8). Early passage telocytes were cultured on ECM of
304 varying stiffness (0.2 kPa (low), 8 kPa (intermediate), and 64 kPa (high), and harvested for bulk
305 RNAseq. The results demonstrated that telocytes retain their *Efhd1* and *Myoc* expression on low
306 stiffness ECM but differentiate into other types of mesenchymal cells, including fibroblasts and
307 myocytes, on stiff matrix (Fig. 9).

308

309 **DISCUSSION**

310 RA is a complex immune-mediated inflammatory disorder with divergent mechanisms of
311 disease progression (*47, 48*). Recent high-dimensional studies of RA tissues revealed multiple
312 cell types and factors that contribute to chronic inflammation in affected joints (*49, 50*), and this
313 knowledge catalyzed promising treatment strategies for RA patients (*51*). Despite these
314 therapeutic advances, major unmet clinical needs remain for a large fraction of RA patients that
315 fail to achieve remission and ~30% who are refractory to all current therapies (*47, 48*). This
316 treatment shortfall underscores the need to find novel disease mechanisms and treatment

317 strategies. With this objective in mind, we focused on the autoimmune independent pathologies
318 of inflammatory-erosive arthritis observed in TNF-tg mice (*52*). This research led to the
319 discovery of the synovial lymphatic system (*53*), an interactive network critical for joint
320 homeostasis (*54*), which is dysfunctional in RA and osteoarthritis, and this altered function
321 correlates with disease progression and flare (*13, 14*). Thus, elucidation of the mechanisms that
322 regulate the synovial lymphatic system and its dysfunction during chronic arthritis opens new
323 avenues of investigation for the development of new therapies. Here we demonstrate that DTA-
324 mediated telocyte deletion inhibits normal lymphatic function (Fig. 6) and exacerbates
325 inflammatory-erosive arthritis (Fig. 7), which raises the possibility that these cells might serve as
326 a novel target for treating RA patients who are refractory to all current therapies.

327 In contrast to the circulatory system, which is responsible for blood flow, and where
328 development, regulation, and repair have been defined in great cellular and molecular detail,
329 many fundamental questions about lymphatics remain unanswered, including the origins of
330 LMCs and cLV maintenance and repair (*3, 55*). Critical questions pertaining to the mechanisms
331 that control cLV contractions also remain unanswered. To address lymphatic contraction
332 mechanisms, Zawieja et al utilized conditional-inducible $CreER^{T2}$ transgenic mice to assess the
333 innate pacemaking potential of mast cells, telocytes, pericytes, fibroblasts and LMCs in cLVs ex
334 vivo (*9*). These studies failed to identify Ca^{++} events in PDGFRα^{+} or c-Kit^{+} adventitial cells that
335 were in phase with cLV contractile activity. These investigators were unable to consistently elicit
336 contractions following optogenetic stimulation via a light-activated cation channel rhodopsin2
337 (ChR2), indicating that adventitial cells (e.g. telocytes) are not spontaneous pacemakers.
338 However, they did find that MYH11^{+} LMCs exhibited asynchronous diastolic Ca^{++} events that
339 were dynamically modulated by pressure, and these cells also propagated contraction in response

340 to ChR2 photo-stimulated depolarization (*9*). Taken together with other studies (*5, 56*), these
341 results support a long-standing model of LMCs as the intrinsic pacemaker of cLVs (*57*). While
342 these studies largely explain the mechanisms responsible for intraluminal pressure-dependent
343 spontaneous cLV contractions, they do not provide information on the initiating signal for distal
344 tissue LMC contractions in response to edema (e.g. joint effusions).

345 In retrospect, our finding that ablation of peri-PLV telocytes is associated with lymphatic
346 dysfunction is not surprising, as pacemaking in smooth muscle-invested organs is known to be
347 controlled by this cell type (*6*). Indeed, pioneering studies of gastrointestinal smooth muscle
348 found that pacemaking is initiated by ICC (*58, 59*), and subsequent studies of the lower urinary
349 tract (*60*), gallbladder (*61*), and oviduct (*62*) found similar cells, now generically referred to as
350 telocytes (*35, 36*). Additionally, cells characteristic of telocytes have been identified in LVs (*63*),
351 and prior studies identified methylene blue staining peri-LV $CD34^+$/c-Kit^+ cells with telocyte
352 morphology and telopode-like structures extending to LMCs (*9, 63*).
353 It also reasons that telocytes are involved in cLV contractions, as LMCs are akin to
354 smooth muscle cells that lack the ionic mechanisms required for action potential regeneration
355 and electrical signals that efficiently propagate between muscle cells (*64*). Thus, LMCs likely
356 rely on a telocyte network for signal conduction. Consistently, telocytes mediate rhythmic
357 electrical activity in other tissues (*65*), which is believed to depend on ion channels for
358 generating pacemaking currents (*66, 67*). Interestingly, electrically coupled cells are typically
359 connected by gap junctions (*63*), and evidence demonstrating this physical link between
360 telocytes and LMCs does not exist (*6*). Studies have also failed to demonstrate functional
361 electrical communication between telocytes and LMCs or a telocyte Ca^{++} clock to drive the
362 rhythmic cLV contractions observed *ex vivo* (*9*). However, it is conceivable, based on our

363 findings, that an intermediary cell provides the depolarizing signals to LMCs to initiate
364 pacemaking, which we posit to be peri-cLV mast cells integrated into telocytes (Fig. 3). Mast
365 cells produce, store, and release various inflammatory and vasoactive mediators (*27, 68*). These
366 mediators influence lymphatic pumping by affecting LMC contractility (*69*), and may be
367 responsible for directly providing the initiating pacemaking signal to LMCs in joint-draining
368 cLV secondary to a Ca^{++} flux through gap junctions from attached telocytes. The Ca^{++} flux
369 generated from telocyte responses to osmotic stress (Figure 8b) and Ehfd1 may play a direct role
370 in calcium signaling via inhibition of the mitochondrial calcium uniporter (*70*), followed by
371 shunting of intracellular Ca^{++} through the telocyte network into mast cells.

372 Our finding that *Myoc* is a peri-PLV telocyte marker gene is also not surprising given that
373 the extensive ECM (Fig. 4d), and primary functions of this protein are cross-linking ECM
374 proteins and regulating MMPs (*71*). It is highly probable that *Myoc* is not a telocyte-specific
375 gene in the joint (Fig. 5b) since the fibroblasts in these musculoskeletal tissues play a major role
376 in ECM genesis and remodeling. Therefore, since *Efhd1*-CreER^{T2} mice have more selective gene
377 targeting, we conclude that they are superior model for telocyte research. However, mutations in
378 the *Myoc* are known to be the greatest genetic risk factor for glaucoma. Thus, the *Myoc*-CreER^{T2}
379 mice may be a useful model to better understand this disease.

380 Here we also report the first evidence of tissue-specific telocytes, which includes our
381 failure to detect *Efhd1* and *Myoc* expression in ICC of the gut (Supplemental Fig. 5a). This
382 observation also distinguishes our *Efhd1* and *Myoc* telocyte-targeted CreER^{T2} models from the
383 established *FoxL1*-Cre targeted models (*43, 72*), although all of these mice have transgene
384 targeting in subepithelial telocytes, suggesting overlaps in the tissue specificity of distinct
385 telocytes. Additionally, our scRNAseq data demonstrates that synovial and peri-PLV telocytes

386 do not express *Ano1* (Fig. 5c), which is considered to be the canonical Ca^{++} activated chloride
387 channel in ICC required for pacemaker activity (*66, 73*). Thus, Ca^{++} signaling in telocytes of the
388 synovial lymphatic system must involve different pathways, which might include mitochondria,
389 considering that EFHD1 regulates mitoflash activation that mediates intercellular signaling (*74*)
390 and physically binds to the mitochondrial calcium uniporter to inhibit the Hippo/YAP pathway
391 and cellular invasives (*70*). Taken together with our findings that *Efhd1* expression in telocytes is
392 lost during telocyte to fibroblast/myofibroblast differentiation (Fig. 9), EFHD1 may be a target to
393 stabilize telocytes in arthritis and other emerging fields that propose telocyte transplantation (*75*).
394 In terms of the well-known fibrosis that is associated with RA and lymphedema, our *in*
395 *vitro* findings demonstrating that relatively non-motile *Efhd1*$^{+}$ telocytes differentiate into
396 invasive fibroblasts in response to TGF-β and stiff ECM (Figs. 8 & 9) may provide etiologic
397 insights. Thus, prospective lineage tracing studies with tamoxifen-treated *Efhd1*-CreER^{T2} x Ai9
398 and *Myoc*-CreER^{T2} x Ai9 mice are warranted to see if this telocyte to myofibroblast
399 differentiation also occurs in vivo, especially in disease models.
400 We present the first report of telocytes within the synovial lymphatic system, coupled
401 with several preliminary findings that must be addressed in future studies. Notable among these
402 limitations are potential off-target effects of our transgenic mouse models when performing
403 systemic tamoxifen delivery experiments. As our models may target cells in tissues that were not
404 studied exhaustively and we confirmed targeting to non-telocytes known to express Efhd1 (e.g.
405 renal tubule cells (*70*) Supplemental Fig. 9), conclusions about telocyte-specific effects need to
406 be tempered. We also report some preliminary results that need to be follow up in future studies.
407 The first is our variable findings of increased osteoclasts in femurs of mice with DTA-deleted
408 target cells (Supplemental Fig. 7), which warrants prospective studies to determine if these

409 preliminary observations are significant. We also conclude that our highly variable NIR-ICG
410 results to assess lymphatic drainage of PBS vs. zymosan injected knees were confounded by
411 effects of multiple intraarticular injections (data not shown), and that faithful measurement of
412 lymphatic drainage from the knee will likely require technical innovations (e.g. assessing large
413 molecule translocation from the joint to iliac lymph nodes).

414 In summary, we find that telocytes embedded in the ECM around PLVs are lost in TNF-
415 tg mice with inflammatory arthritis, and telocyte networks adjacent to PLVs are integrated into
416 mast cells. Furthermore, telocyte deletion decreases lymphatic function and exacerbates ZIA.
417 Based on these discoveries, we propose a unifying model to explain the functions of telocytes
418 within the synovial lymphatic system (Fig. 10). This model posits three testable hypotheses that
419 are the focus of our future directions. The first is the existence of connected telocyte networks
420 that parallel lymphatic vessels from the synovial lymphatic capillaries to mast cell elaborated
421 cLV, which is supported by our WMIFM images (Fig. 2h) and can be further tested by high
422 resolution light-sheet microscopy to confirm the tdT^{+} cells in the array are physically associated.
423 The second is that telocytes sense osmotic pressure in joints (e.g. ankle) and signal through the
424 telocyte network to the peri-PLV mast cells that degranulate and initiate LMC contractions in
425 response. Experiments to test this will require generation of double transgenic mice in which the
426 *Efhd1*-$CreER^{T2}$ are crossed to mice with telocyte or mast cell specific Ca^{++} reporter probes for
427 intravital microscopy studies following ankle stimulations. Finally, we propose that RA-FLS are
428 derived from telocytes that differentiate in response to chronic inflammation and adherence to
429 rigid ECM in inflamed joints. This could be tested via lineage tracing studies with tamoxifen-
430 treated *Efhd1*-$CreER^{T2}$ x Ai9 mice, and genetic EFHD1 gain and loss of function studies, which

431 could provide the field with a novel molecular target to treat pauci-immune RA and lymphedema
432 that is refractory to all known treatments.

433

434 **Methods**

435 **Mouse models.** All animal research was conducted with approval by the University of Rochester
436 Institutional Animal Care and Use Committee. Three transgenic mouse strains were generated
437 with P2A-CreER^{T2} cassettes, which were knocked into C57BL/6NTac mice via CRISPR/Cas-
438 mediated genome engineering (Taconic Biosciences, Germantown, NY). Cas9 and gRNA were
439 co-injected into fertilized eggs with the targeting vector, and the resulting pups were genotyped
440 by PCR followed by Sanger sequencing analysis to confirm the precise insertion loci (for primers
441 see Table 1). For the Efhd1-CreER^{T2} model, the TAG stop codon in the mouse *Efhd1* gene
442 (NCBI Reference Sequence: NM_028889.3) was replaced by a "P2A-CreER^{T2}" cassette
443 (Transcript: 201-ENSMUST00000027472). A synonymous mutation p. R232= (CGG to AGA)
444 was also introduced to prevent the binding and re-cutting of the sequence by gRNA after
445 homology-directed repair. For the Myoc-CreER^{T2} model, the TGA stop codon in the mouse
446 *Myoc* gene (NCBI Reference Sequence: NM_010865.3) was replaced by a "P2A-CreER^{T2}"
447 cassette (Transcript: 201-ENSMUST00000028020). For the Pla1a-CreER^{T2} model, the TGA stop
448 codon in the mouse *Pla1a* gene (NCBI Reference Sequence: NM_134102.4) was replaced by a
449 "P2A-CreER^{T2}" cassette (Transcript: 201-ENSMUST00000002926).

450 B6.Cg-*Gt(ROSA)26Sor*$^{tm9(CAG\text{-}tdTomato)Hze}$/J (Ai9)(*33*), B6.129P2-
451 *Gt(ROSA)26Sor*$^{tm1(DTA)Lky}$/J (DTA)(*34*) and B6.Cg-*Kit*$^{W\text{-}sh}$ /HNihrJaeBsmJ (*Kit*$^{W\text{-}sh/W\text{-}sh}$ or cKit$^{-/-}$)

452 mice were purchased from The Jackson Laboratory (Bar Harbor, ME, Ai9 Strain #:007909, DTA
453 Strain #:009669, Kit Strain #: 030764) and maintained at the University of Rochester vivarium.
454 For crossing between the strains, $CreER^{T2}$ conditional inducible mice were used as male
455 breeders, and Ai9 or DTA mice as female breeders. For all *in vivo* longitudinal outcome
456 measures, mice were anesthetized with 1–3% isoflurane. All mice were euthanized with a lethal
457 dose of ketamine/xylazine cocktail (intraperitoneal) followed by cervical dislocation.

458 **Whole mount immunofluorescent microscopy (WMIFM).** PLVs were harvested and fixed as
459 previous described(*76*). Briefly, fixed PLVs were blocked with 5% normal goat serum (NGS;
460 ThermoFisher Scientific Cat# 50062Z)/1 × TBS/0.3% Triton X-100 for 1 hr at RT, and then
461 incubated with the primary antibodies diluted in 5% NGS/1 × TBS / 0.3% Triton X-100
462 overnight at 4 °C. For αSMA labeling, primary antibodies include mouse anti-αSMA antibody
463 (AlexaFluor 488 conjugate; ThermoFisher Scientific Cat# 53-9760-82, diluted at 1:100). To
464 validate the mast cell-telocyte interaction, the following primary antibodies targeting mast cells
465 were used in this study: Rabbit anti-human Mast Cell Tryptase IgG (mouse reactivity; Bioss
466 Antibodies Cat# BSM-52533R; 1:100 dilution). To prevent non-specific labeling of Fc receptors
467 (FcR), exclusively secondary antibodies below featuring F(ab) fragments were employed: Anti-
468 rabbit IgG (H+L), F(ab')2 Fragment (Alexa Fluor® 647 Conjugate; Cell Signaling Technology
469 Cat#4414; 1:500 dilution). After 3 × 10 min washes in 1 × TBS/0.1% Triton X-100 following
470 antibody incubation, the PLVs were mounted on a microscope slide with one drop of both
471 ProLong Gold Antifade Mountant (ThermoFisher Scientific Cat# P36930) and NucBlue Fixed
472 ReadyProbes Reagent (DAPI formulation; ThermoFisher Scientific Cat# R37606). The PLVs
473 were then imaged using a VS120 Slide Scanner for αSMA coverage analysis and Nikon A1R HD
474 confocal microscopy as previously described (*31, 76*).

475 To validate the mast cell-telocyte interaction, the following primary antibodies targeting
476 mast cell were used in this study: Rabbit anti-human Mast Cell Tryptase IgG (mouse reactivity;
477 Bioss Antibodies Cat# BSM-52533R; 1:100 dilution). To prevent non-specific labeling of Fc
478 receptors (FcR), exclusively secondary antibodies below featuring F(ab) fragments were
479 employed: Anti-rabbit IgG (H+L), F(ab')2 Fragment (Alexa Fluor® 647 Conjugate; Cell
480 Signaling Technology Cat#4414; 1:500 dilution). After 3 × 10 min washes in 1 × TBS/0.1%
481 Triton X-100 following antibody incubation, the PLVs were mounted on a microscope slide with
482 one drop of both ProLong Gold Antifade Mountant (ThermoFisher Scientific Cat# P36930) and
483 NucBlue Fixed ReadyProbes Reagent (DAPI formulation; ThermoFisher Scientific Cat#
484 R37606). The PLVs were then imaged using a VS120 Slide Scanner for αSMA coverage
485 analysis and Nikon A1R HD confocal microscopy as previously described(*26*).

486 To confirm telocyte identity and characterize marker expression, whole-mounted
487 lymphatic vessels, OCT-frozen cryosections, or paraffin-embedded tissue sections were
488 subjected to immunofluorescence staining. The following primary antibodies were used: anti-
489 CD34 antibody (Abcam Cat# ab81289; 1:50 dilution), CD31 Monoclonal Antibody (Thermo
490 Fisher Cat# MA1-40074; 1:50), anti-COMP (Abcam Cat# ab231977; 1:125), CD117 (c-Kit)
491 Monoclonal Antibody (Thermo Fisher Cat# 14-1172-81; 1:100), and anti-Myocilin (Abcam Cat#
492 ab41552; 1:50). To prevent non-specific Fc receptor binding, only secondary antibodies with
493 $F(ab')_2$ fragments were used: Alexa Fluor® 647–conjugated anti-rabbit IgG (Cell Signaling
494 Technology Cat# 4414; 1:500), Alexa Fluor® 555–conjugated anti-rabbit IgG (Cell Signaling
495 Technology Cat# 4413; 1:1000), FITC-conjugated goat anti-rat IgG (Jackson ImmunoResearch
496 Cat# 112-096-003; 1:200), Alexa Fluor® 647–conjugated donkey anti-rat IgG (Jackson
497 ImmunoResearch Cat# 712-606-153; 1:500), and FITC-conjugated goat anti-rabbit IgG (Jackson

498 ImmunoResearch Cat# 111-096-047; 1:100). Washing, mounting, and imaging were performed
499 as described above.

500 **Cryosection preparation and Immunohistochemistry (IHC).** Mice were anesthetized with
501 ketamine (100 mg/kg) and xylazine (10 mg/kg) prior to cardiac perfusion with PBS followed by
502 4% paraformaldehyde (PFA). Tissues of interest were harvested and fixed in 10% neutral
503 buffered formalin (NBF) for 3 days at room temperature. After fixation, tissues were washed
504 three times in PBS and equilibrated in 40% sucrose at 4 °C overnight. Tissues were then
505 infiltrated with optimal control temperature (OCT) embedding medium for 30 minutes at room
506 temperature, transferred to fresh OCT, and snap-frozen for cryosectioning. Frozen blocks were
507 sectioned at 10 µm thickness and collected onto glass slides. Sections were used directly to
508 assess tdT^+ endogenous expression via fluorescent microscopy or processed for IHC using the
509 same antibodies described above for WHIFM.

510 **Histochemistry and Histomorphometry.** For histochemistry of ankles and knees and
511 quantification of synovitis and osteoclasts, lower limbs of the mice were processed for paraffin
512 embedded demineralized hematoxylin and eosin (H & E) as previously described (*22*). All slides
513 were scanned with an Olympus VS120 (full slide scans available upon request), and
514 histomorphometry for synovial area was quantified with Visiopharm (Hoersholm, Denmark) as
515 previously described (*77*).

516 **Electron microscopy.** Transmission electron microscopy (TEM) was performed as previously
517 described (*20*). The afferent lymphatic vessel to the PLN was identified by injecting Evan's blue
518 in the footpad and was then excised and fixed overnight at 4ºC using a combination fixative of
519 2.5% glutaraldehyde and 4% paraformaldehyde in 0.1M sodium cacodylate buffer for 24 hours.

520 The specimens were rinsed in 0.1M sodium cacodylate buffer and post-fixed with buffered 1%
521 osmium tetroxide. The tissue was dehydrated in a graded series of ethanol to 100%, transitioned
522 into propylene oxide, infiltrated with EPON/Araldite epoxy resin, followed by embedment in fresh
523 resin and polymerization for 2 days at 70ºC. To identify the lymphatic vessel in the specimen, the
524 epoxy embedded block was cut serially into 1µm sections and stained with Toluidine blue. Then
525 the specimen block was trimmed of excess surrounding tissue and thin sectioned at 70 nm with a
526 diamond knife using an ultramicrotome. The thin sections were placed onto 150 mesh carbon
527 coated nickel slot grids and stained with uranyl acetate and lead citrate. A Hitachi 7650
528 Transmission Electron Microscope with a Gatan 11-megapixel Erlangshen digital camera was used
529 to image the grids. Scanning electron microscopy (SEM) was performed, as previously
530 described.(*26*) Briefly, PLVs were fixed in 2.5% glutaraldehyde/4% paraformaldehyde/0.1M
531 cacodylate overnight, post-fixed in buffered 1% osmium tetroxide, dehydrated, critically point
532 dried, mounted onto aluminum stubs and sputter coated with gold prior to imaging using a Zeiss
533 Auriga FE SEM. Three SEM micrographs per sample group were randomly chosen for descriptive
534 analysis.

535

536 **Single-cell RNA sequencing analyses.** *In silico* analyses of previously published scRNAseq
537 datasets of WT and TNF-tg PLV (GEO; accession number GSE190999) (*32*) were performed
538 using Seurat (v5.0.1) to generate UMAPs of the mesenchymal cells. Individual gene expression
539 within this UMAP was performed with FeaturePlot in Seurat. Pseudotime predictions analysis of
540 the scRNAseq data from WT and TNF-tg PLV was performed with Monocle 3 to generate UMAPs
541 with heatmaps of the hypothesized cellular differentiation and the telocytes:fibroblasts ratio. For
542 *de novo* scRNAseq of synoviocytes, knee tissue from tamoxifen-treated *Efhd1*CreER x Ai9 mice

543 was digested into a single-cell suspension and processed for scRNAseq as previously
544 described(*32*). RNA-seq libraries were prepared using the NEBNext® Ultra™ II RNA Library
545 Prep Kit plus tdT and sequenced on an Illumina NovaSeq X Plus platform. Reads were aligned to
546 the Mus musculus reference genome (GRCm39) using STAR. UMAPs were generated from the
547 sequence data (GEO; accession number GSE303999) to identify unique cell clusters and
548 expression of marker genes.

549

550 **Bulk RNAseq of purified telocyte cultures on stiffness-defined substrates.** Telocytes were
551 isolated from the ankle synovium of tamoxifen-treated *Efhd1*CreER x Ai9 mice, and tdT^+ cells
552 were FACS purified and plated onto collagen type I–coated CytoSoft® 24-well plates (Advanced
553 BioMatrix, Cat#5183, #5186, #5189) with defined stiffness levels of 0.2, 8, or 64 kPa. After 24
554 hours of culture, cells were lysed directly in Buffer RLT Plus (Qiagen, Cat#1053393), and total
555 RNA was extracted using the RNeasy Plus Micro Kit (Qiagen, Cat# 74134) following the
556 manufacturer's instructions. RNA-seq libraries were prepared using the NEBNext® Ultra™ II
557 RNA Library Prep Kit and sequenced on an Illumina NovaSeq X Plus platform. Reads were
558 aligned to the Mus musculus reference genome (GRCm39) using STAR (GEO; accession number
559 GSE303624). Differential expression analysis was performed using DESeq2, and visualization of
560 gene expression patterns was conducted using the Seurat package (v5.0.1).

561

562 **Near infrared-indocyanine (NIR-ICG) imaging and quantification of lymphatic function.**
563 The subcutaneous injection of 10 µl of a 0.1 mg/ml ICG solution in water was administered to
564 both hind footpads of the mouse. The fluorescence of the footpad was measured in an IVIS Live

565 Animal Imaging System (Caliper Life Sciences Inc.) one hour after injection (baseline) to
566 capture the maximum fluorescence signal intensity, and again at six hours to quantify the
567 remaining fluorescence signals that were not drained away by lymphatic flow. The ratio of the
568 fluorescence difference and baseline fluorescence was used to define lymphatic clearance
569 function, which reflects the lymphatic vessel's ability to remove extra fluid from the footpad.

570 **Zymosan-induced arthritis (ZIA) model.** Female 8-weeks-old *Efhd1*-CreER$^{+/-}$ x DTA$^{f/-}$ mice
571 and wild-type littermate controls received intraperitoneal injections of tamoxifen (0.1 mg/g body
572 weight) for 5 consecutive days to induce *Efhd1*-driven DTA expression and telocyte depletion.
573 Two weeks after the initiation of tamoxifen treatment, mice were anesthetized and received a
574 single intra-articular injection of 180 µg zymosan (Sigma-Aldrich, St. Louis, MO, USA) in 6 µL
575 PBS into the knee joint cavity. Control mice received PBS alone. Knee joint inflammation was
576 monitored by high-resolution ultrasound imaging (Vevo 3100, VisualSonics) performed before
577 zymosan injection (baseline) and on days 2, 7, and 14 post-injection. Analysis of knee joint
578 inflammation was performed using Amira to measure synovial volume, as described before. (*78*)
579 On days 13–15, mice were euthanized, and knee joints were harvested, fixed in 4%
580 paraformaldehyde, micro-CT scanned, and processed for histological analysis.

581

582 **Micro-CT analysis.** Micro-CT scanning and 3D reconstruction were performed as previously
583 described(*79*), using identical imaging settings and parameters. Following reconstruction, femurs
584 were digitally segmented from adjacent skeletal structures to improve visualization. To assess
585 articular erosions, 2D projections were generated from the articular surface of the femoral trochlea,
586 which articulates with the tibia. This approach maximized the visualization of surface erosion in a

587 flattened plane and minimized distortion-related quantification errors. Erosive lesions were
588 manually annotated using QuPath (v0.5.0), and the cumulative erosion area was normalized to the
589 total projected area of the distal femur (ROI). The erosion percentage (erosion area/ROI) was used
590 as a quantitative measure of joint damage.

591

592 **In vitro cellular invasion assays with 3D confocal microscopy and image reconstruction.**
593 Matrigel invasion assays were performed using transwell inserts containing cells suspended in
594 serum-free medium. Cells migrated toward a bottom chamber containing 10% fetal bovine serum
595 (FBS), with or without 5 ng/mL TGF-β, for 24 hours. Cultures were then stained with Hoechst to
596 label nuclei and imaged using an inverted Nikon Ti2-E confocal fluorescence microscopy.
597 Representative 3D reconstructions were generated and analyzed using Imaris (version 10.2 Oxford
598 Instruments). For quantitative analysis, the centroid of each Hoechst-stained nucleus was used to
599 define the position of individual cells. Cells were classified as *Efhd1*$^{+}$ telocytes if their nuclei were
600 spatially enclosed within the tdTomato signal, or as *Efhd1*$^{-}$ fibroblasts if there was no overlap with
601 tdTomato fluorescence. The shallowest nucleus, typically corresponding to a non-migratory or
602 dead cell, was defined as the reference surface level. The vertical distance between each nucleus
603 and this reference plane was calculated as the invasion depth. Distributions of invasion depth were
604 quantified across three independent experiments.

605

606 ***Ex vivo* co-culture and assays for osmotic pressure response and migration.** PLVs with
607 surrounding adipose tissue were harvested from *Myoc*-CreER x Ai9 or *Efhd1*-CreER x Ai9
608 reporter mice and cultured in DMEM + 10% FBS (Sigma-Aldrich, St. Louis, MO, USA) to

609 establish monolayer co-cultures of tdT^+ telocytes and unlabeled tdT^- fibroblasts. For
610 immunostaining, cells were seeded into the Nunc™ Lab-Tek™ II Chamber Slide™ System
611 (Thermo Fisher Scientific, Cat# 154534PK), fixed with 10% NBF, and the plastic chamber was
612 removed prior to staining. Subsequent staining procedures followed the same protocol as for
613 tissue cryosections. For osmotic shock studies, the primary cells were loaded with Hoechst
614 nuclear stain (Invitrogen, Waltham, MA) and 10 μM Fluo-4 (Invitrogen, Waltham, MA) as
615 previously described (*80*). After 30 minutes of incubation, cells were supplemented with 10 mM
616 Ca^{++} and stimulated with varying concentrations of sucrose (6.25-800 μM) to induce
617 hyperosmotic pressure changes. Real-time fluorescent microscopy was performed to track Ca^{++}
618 influx responses. The percentage of responsive cells was calculated by normalizing the number
619 of Fluo-4^+ tdT^+ $Hoechst^+$ cells to total tdT^+ $Hoechst^+$ cells for telocytes, and Fluo-4^+ tdT^-
620 $Hoechst^+$ cells to total tdT^- $Hoechst^+$ cells for fibroblasts.

621 **Statistics.** All statistical analyses were performed using GraphPad Prism (version 9.1.1,
622 GraphPad Software, Boston, MA, USA) and R (version 4.3.2). Additional analyses and data
623 visualization, including quantification of osmotic shock assay, invasion assays and ZIA model
624 readouts were conducted using the R packages ggpubr (version 0.6.0). Two-group comparisons
625 were assessed using unpaired two-tailed Student's t-tests, and multiple group comparisons were
626 performed using one-way or two-way ANOVA as appropriate. A *p*-value less than 0.05 was
627 considered statistically significant.

628 **Data availability**

629 The data that support the findings of this study are available upon request. Source data are
630 available for Figs. 3c & g, 4b, 5d & f, 6c-f, 9b-c, 10a. The RNA-sequencing datasets have been

631 deposited in GEO database under accession code GSE303999 (scRNA-seq of telocytes in
632 synovial tissue) and GSE303624 (bulk RNA-seq of telocytes cultured under different matrix
633 stiffness conditions).
634

635 **Acknowledgements**

636 We would like to thank the faculty and staff at the Genomics Research Center and Histology,
637 Biochemistry, Electron Microscopy Resource in the Center for Advanced Resource
638 Technologies, and Molecular Imaging Core at the University of Rochester Medical Center. This
639 work was supported by funding from the National Institutes of Health: F30 AG069329 (HMK),
640 T32GM007356 (HMK), R01AR063650, R01AG059775 (LX), R01AR069000 (CTR),
641 R01AR056702 (EMS), and P30 AR069655 (EMS).

642

643 **References**

644 1. B. J. Mehrara *et al.*, The emerging importance of lymphatics in health and disease: an NIH
645 workshop report. *J. Clin. Invest.* **133**, (2023).
646 2. D. Negrini, Morphological, Mechanical and Hydrodynamic Aspects of Diaphragmatic Lymphatics.
647 *Biology (Basel)* **11**, (2022).
648 3. J. P. Scallan, S. D. Zawieja, J. A. Castorena-Gonzalez, M. J. Davis, Lymphatic pumping: mechanics,
649 mechanisms and malfunction. *J. Physiol.* **594**, 5749-5768 (2016).
650 4. A. R. Hargens, B. W. Zweifach, Contractile stimuli in collecting lymph vessels. *Am. J. Physiol.* **233**,
651 H57-65 (1977).
652 5. S. D. Zawieja *et al.*, Ano1 mediates pressure-sensitive contraction frequency changes in mouse
653 lymphatic collecting vessels. *J. Gen. Physiol.* **151**, 532-554 (2019).
654 6. M. J. Davis, S. D. Zawieja, Pacemaking in the lymphatic system. *J. Physiol.*, (2024).
655 7. Q. Zhou, R. Wood, E. M. Schwarz, Y. J. Wang, L. Xing, Near-infrared lymphatic imaging
656 demonstrates the dynamics of lymph flow and lymphangiogenesis during the acute versus
657 chronic phases of arthritis in mice. *Arthritis Rheum.* **62**, 1881-1889 (2010).
658 8. J. P. Scallan *et al.*, Independent and interactive effects of preload and afterload on the pump
659 function of the isolated lymphangion. *Am. J. Physiol. Heart Circ. Physiol.* **303**, H809-824 (2012).
660 9. S. D. Zawieja *et al.*, Characterization of the cellular components of mouse collecting lymphatic
661 vessels reveals that lymphatic muscle cells are the innate pacemaker cells regulating lymphatic
662 contractions. *eLife*, https://doi.org/10.7554/eLife.90679.90672 (2024).
663 10. M. J. Davis, C. D. Bertram, Control of lymphatic pacemaking and pumping by mechanobiological
664 signals. *J. Physiol.*, (2025).
665 11. M. Muthuchamy, A. Gashev, N. Boswell, N. Dawson, D. Zawieja, Molecular and functional
666 analyses of the contractile apparatus in lymphatic muscle. *FASEB J.* **17**, 920-922 (2003).
667 12. S. H. Azhar, H. Y. Lim, B. K. Tan, V. Angeli, The Unresolved Pathophysiology of Lymphedema.
668 *Front. Physiol.* **11**, 137 (2020).
669 13. E. M. Bouta *et al.*, Targeting lymphatic function as a novel therapeutic intervention for
670 rheumatoid arthritis. *Nat Rev Rheumatol* **14**, 94-106 (2018).
671 14. M. Cao, M. T. Y. Ong, P. S. H. Yung, R. S. Tuan, Y. Jiang, Role of synovial lymphatic function in
672 osteoarthritis. *Osteoarthritis Cartilage* **30**, 1186-1197 (2022).
673 15. Q. Zhang *et al.*, VEGF-C, a Lymphatic Growth Factor, Is a RANKL Target Gene in Osteoclasts That
674 Enhances Osteoclastic Bone Resorption through an Autocrine Mechanism. *J. Biol. Chem.* **283**,
675 13491-13499 (2008).
676 16. R. Guo *et al.*, Inhibition of lymphangiogenesis and lymphatic drainage via vascular endothelial
677 growth factor receptor 3 blockade increases the severity of inflammation in a mouse model of
678 chronic inflammatory arthritis. *Arthritis Rheum.* **60**, 2666-2676 (2009).
679 17. Q. Zhou *et al.*, Vascular endothelial growth factor C attenuates joint damage in chronic
680 inflammatory arthritis by accelerating local lymphatic drainage in mice. *Arthritis Rheum.* **63**,
681 2318-2328 (2011).
682 18. S. T. Proulx *et al.*, MRI and quantification of draining lymph node function in inflammatory
683 arthritis. *Ann. N. Y. Acad. Sci.* **1117**, 106-123 (2007).
684 19. J. Li *et al.*, Expanded CD23(+)/CD21(hi) B cells in inflamed lymph nodes are associated with the
685 onset of inflammatory-erosive arthritis in TNF-transgenic mice and are targets of anti-CD20
686 therapy. *J Immunol* **184**, 6142-6150 (2010).

687 20. E. M. Bouta *et al.*, Treatment of Tumor Necrosis Factor-Transgenic Mice With Anti-Tumor
688 Necrosis Factor Restores Lymphatic Contractions, Repairs Lymphatic Vessels, and May Increase
689 Monocyte/Macrophage Egress. *Arthritis Rheumatol* **69**, 1187-1193 (2017).
690 21. J. Li *et al.*, Efficacy of B cell depletion therapy for murine joint arthritis flare is associated with
691 increased lymphatic flow. *Arthritis Rheum.* **65**, 130-138 (2012).
692 22. R. D. Bell *et al.*, iNOS dependent and independent phases of lymph node expansion in mice with
693 TNF-induced inflammatory-erosive arthritis. *Arthritis Res Ther* **21**, 240 (2019).
694 23. H. M. Kenney *et al.*, Multi-omics analysis identifies IgG2b class-switching with ALCAM-CD6 co-
695 stimulation in joint-draining lymph nodes during advanced inflammatory-erosive arthritis. *Front*
696 *Immunol* **14**, 1237498 (2023).
697 24. R. D. Bell *et al.*, Altered Lymphatic Vessel Anatomy and Markedly Diminished Lymph Clearance
698 in Affected Hands of Patients With Active Rheumatoid Arthritis. *Arthritis Rheumatol* **72**, 1447-
699 1455 (2020).
700 25. J. P. Scallan *et al.*, Ex vivo Demonstration of Functional Deficiencies in Popliteal Lymphatic
701 Vessels From TNF-Transgenic Mice With Inflammatory Arthritis. *Front. Physiol.* **12**, 745096
702 (2021).
703 26. H. M. Kenney *et al.*, Persistent popliteal lymphatic muscle cell coverage defects despite
704 amelioration of arthritis and recovery of popliteal lymphatic vessel function in TNF-Tg mice
705 following anti-TNF therapy. *Scientific Reports* **12**, 12751 (2022).
706 27. S. Pal, S. Nath, C. J. Meininger, A. A. Gashev, Emerging Roles of Mast Cells in the Regulation of
707 Lymphatic Immuno-Physiology. *Front. Immunol.* **11**, 1234 (2020).
708 28. P. A. Nigrovic, D. M. Lee, Mast cells in inflammatory arthritis. *Arthritis Res Ther* **7**, 1 (2004).
709 29. F. Rivellese *et al.*, Mast cells in early rheumatoid arthritis associate with disease severity and
710 support B cell autoantibody production. *Ann Rheum Dis* **77**, 1773-1781 (2018).
711 30. J. Keffer *et al.*, Transgenic mice expressing human tumour necrosis factor: a predictive genetic
712 model of arthritis. *EMBO J.* **10**, 4025-4031 (1991).
713 31. Y. Peng *et al.*, Distinct mast cell subpopulations within and around lymphatic vessels regulate
714 lymph flow and progression of inflammatory-erosive arthritis in TNF-transgenic mice. *Front.*
715 *Immunol.* **14**, 1275871 (2023).
716 32. H. M. Kenney *et al.*, Single-cell transcriptomics of popliteal lymphatic vessels and peripheral
717 veins reveals altered lymphatic muscle and immune cell populations in the TNF-Tg arthritis
718 model. *Arthritis Res Ther* **24**, 64 (2022).
719 33. L. Madisen *et al.*, A robust and high-throughput Cre reporting and characterization system for
720 the whole mouse brain. *Nat. Neurosci.* **13**, 133-140 (2010).
721 34. D. Voehringer, H. E. Liang, R. M. Locksley, Homeostasis and effector function of lymphopenia-
722 induced "memory-like" T cells in constitutively T cell-depleted mice. *J. Immunol.* **180**, 4742-4753
723 (2008).
724 35. L. M. Popescu, M. S. Faussone-Pellegrini, TELOCYTES - a case of serendipity: the winding way
725 from Interstitial Cells of Cajal (ICC), via Interstitial Cajal-Like Cells (ICLC) to TELOCYTES. *J Cell Mol*
726 *Med* **14**, 729-740 (2010).
727 36. A. Kondo, K. H. Kaestner, Emerging diverse roles of telocytes. *Development* **146**, (2019).
728 37. I. Rosa *et al.*, Impairment in the telocyte/CD34(+) stromal cell network in human rheumatoid
729 arthritis synovium. *J Cell Mol Med* **25**, 2274-2278 (2021).
730 38. S. I. Paerregaard *et al.*, The small and large intestine contain related mesenchymal subsets that
731 derive from embryonic Gli1(+) precursors. *Nat Commun* **14**, 2307 (2023).
732 39. S. Onuora, Rheumatoid arthritis: RA synovium harbours distinct fibroblast subsets. *Nat Rev*
733 *Rheumatol* **14**, 250 (2018).

734 40. F. Mizoguchi *et al.*, Functionally distinct disease-associated fibroblast subsets in rheumatoid
735 arthritis. *Nat Commun* **9**, 789 (2018).
736 41. P. Lertkiatmongkol, D. Liao, H. Mei, Y. Hu, P. J. Newman, Endothelial functions of
737 platelet/endothelial cell adhesion molecule-1 (CD31). *Curr. Opin. Hematol.* **23**, 253-259 (2016).
738 42. A. Saalbach, U. Anderegg, Thy-1: more than a marker for mesenchymal stromal cells. *FASEB J.*
739 **33**, 6689-6696 (2019).
740 43. M. Shoshkes-Carmel *et al.*, Subepithelial telocytes are an important source of Wnts that
741 supports intestinal crypts. *Nature* **557**, 242-246 (2018).
742 44. P. J. Gomez-Pinilla *et al.*, Ano1 is a selective marker of interstitial cells of Cajal in the human and
743 mouse gastrointestinal tract. *Am. J. Physiol. Gastrointest. Liver Physiol.* **296**, G1370-1381 (2009).
744 45. E. Bernotiene *et al.*, Delayed resolution of acute inflammation during zymosan-induced arthritis
745 in leptin-deficient mice. *Arthritis Res. Ther.* **6**, R256-263 (2004).
746 46. B. M. Radu *et al.*, Calcium Signaling in Interstitial Cells: Focus on Telocytes. *Int J Mol Sci* **18**,
747 (2017).
748 47. E. M. Gravallese, G. S. Firestein, Rheumatoid Arthritis - Common Origins, Divergent Mechanisms.
749 *N. Engl. J. Med.* **388**, 529-542 (2023).
750 48. S. Alivernini, G. S. Firestein, I. B. McInnes, The pathogenesis of rheumatoid arthritis. *Immunity*
751 **55**, 2255-2270 (2022).
752 49. F. Zhang *et al.*, Defining inflammatory cell states in rheumatoid arthritis joint synovial tissues by
753 integrating single-cell transcriptomics and mass cytometry. *Nat. Immunol.* **20**, 928-942 (2019).
754 50. K. Wei *et al.*, Notch signalling drives synovial fibroblast identity and arthritis pathology. *Nature*
755 **582**, 259-264 (2020).
756 51. E. C. Keystone, J. Smolen, P. van Riel, Developing an effective treatment algorithm for
757 rheumatoid arthritis. *Rheumatology (Oxford)* **51 Suppl 5**, v48-54 (2012).
758 52. P. Li, E. M. Schwarz, The TNF-alpha transgenic mouse model of inflammatory arthritis. *Springer*
759 *Semin. Immunopathol.* **25**, 19-33 (2003).
760 53. Q. Liang *et al.*, Lymphatic muscle cells contribute to dysfunction of the synovial lymphatic
761 system in inflammatory arthritis in mice. *Arthritis Res. Ther.* **23**, 58 (2021).
762 54. E. M. Bouta *et al.*, The role of the lymphatic system in inflammatory-erosive arthritis. *Semin Cell*
763 *Dev Biol* **38**, 90-97 (2015).
764 55. H. M. Kenney *et al.*, The Enigmas of Lymphatic Muscle Cells: Where Do They Come From, How
765 Are They Maintained, and Can They Regenerate? *Curr Rheumatol Rev*, (2023).
766 56. J. A. Castorena-Gonzalez, J. P. Scallan, M. J. Davis, Methods for Assessing the Contractile
767 Function of Mouse Lymphatic Vessels Ex Vivo. *Methods Mol. Biol.* **1846**, 229-248 (2018).
768 57. D. F. Van Helden, J. Zhao, Lymphatic vasomotion. *Clin. Exp. Pharmacol. Physiol.* **27**, 1014-1018
769 (2000).
770 58. G. D. Hirst, S. M. Ward, Interstitial cells: involvement in rhythmicity and neural control of gut
771 smooth muscle. *J. Physiol.* **550**, 337-346 (2003).
772 59. Y. Kito, S. M. Ward, K. M. Sanders, Pacemaker potentials generated by interstitial cells of Cajal in
773 the murine intestine. *Am. J. Physiol. Cell Physiol.* **288**, C710-720 (2005).
774 60. B. H. Koh *et al.*, Platelet-derived growth factor receptor-alpha cells in mouse urinary bladder: a
775 new class of interstitial cells. *J. Cell. Mol. Med.* **16**, 691-700 (2012).
776 61. B. Lavoie, O. B. Balemba, M. T. Nelson, S. M. Ward, G. M. Mawe, Morphological and
777 physiological evidence for interstitial cell of Cajal-like cells in the guinea pig gallbladder. *J.*
778 *Physiol.* **579**, 487-501 (2007).
779 62. R. E. Dixon *et al.*, Electrical slow waves in the mouse oviduct are dependent upon a calcium
780 activated chloride conductance encoded by Tmem16a. *Biol. Reprod.* **86**, 1-7 (2012).

781 63. D. Briggs Boedtkjer *et al.*, Identification of interstitial Cajal-like cells in the human thoracic duct.
782 *Cells Tissues Organs* **197**, 145-158 (2013).
783 64. K. M. Sanders, L. F. Santana, S. A. Baker, Interstitial cells of Cajal - pacemakers of the
784 gastrointestinal tract. *J. Physiol.*, (2023).
785 65. R. E. Dixon *et al.*, Chlamydia infection causes loss of pacemaker cells and inhibits oocyte
786 transport in the mouse oviduct. *Biol. Reprod.* **80**, 665-673 (2009).
787 66. S. J. Hwang *et al.*, Expression of anoctamin 1/TMEM16A by interstitial cells of Cajal is
788 fundamental for slow wave activity in gastrointestinal muscles. *J. Physiol.* **587**, 4887-4904
789 (2009).
790 67. S. A. Baker *et al.*, Role of TREK-1 potassium channel in bladder overactivity after partial bladder
791 outlet obstruction in mouse. *J. Urol.* **183**, 793-800 (2010).
792 68. J. P. Scallan, M. J. Davis, Itching for answers: how histamine relaxes lymphatic vessels.
793 *Microcirculation* **21**, 575-577 (2014).
794 69. K. J. Plaku, P. Y. von der Weid, Mast cell degranulation alters lymphatic contractile activity
795 through action of histamine. *Microcirculation* **13**, 219-227 (2006).
796 70. K. Meng *et al.*, EFHD1, a novel mitochondrial regulator of tumor metastasis in clear cell renal cell
797 carcinoma. *Cancer Sci* **114**, 2029-2040 (2023).
798 71. H. Wang *et al.*, Physiological function of myocilin and its role in the pathogenesis of glaucoma in
799 the trabecular meshwork (Review). *Int. J. Mol. Med.* **43**, 671-681 (2019).
800 72. H. M. Kolev *et al.*, A FoxL1-CreERT-2A-tdTomato Mouse Labels Subepithelial Telocytes. *Cell Mol*
801 *Gastroenterol Hepatol* **12**, 1155-1158 e1154 (2021).
802 73. R. D. Singh *et al.*, Ano1, a Ca2+-activated Cl- channel, coordinates contractility in mouse
803 intestine by Ca2+ transient coordination between interstitial cells of Cajal. *J. Physiol.* **592**, 4051-
804 4068 (2014).
805 74. T. Hou *et al.*, Identification of EFHD1 as a novel Ca(2+) sensor for mitoflash activation. *Cell*
806 *Calcium* **59**, 262-270 (2016).
807 75. M. Klein, M. Csobonyeiova, S. Ziaran, L. Danisovic, I. Varga, Cardiac Telocytes 16 Years on-What
808 Have We Learned So Far, and How Close Are We to Routine Application of the Knowledge in
809 Cardiovascular Regenerative Medicine? *Int J Mol Sci* **22**, (2021).
810 76. H. M. Kenney *et al.*, Lineage tracing reveals evidence of a popliteal lymphatic muscle progenitor
811 cell that is distinct from skeletal and vascular muscle progenitors. *Sci Rep* **10**, 18088 (2020).
812 77. R. D. Bell *et al.*, Selective Sexual Dimorphisms in Musculoskeletal and Cardiopulmonary
813 Pathologic Manifestations and Mortality Incidence in the Tumor Necrosis Factor-Transgenic
814 Mouse Model of Rheumatoid Arthritis. *Arthritis Rheumatol* **71**, 1512-1523 (2019).
815 78. E. M. Bouta *et al.*, Power Doppler ultrasound phenotyping of expanding versus collapsed
816 popliteal lymph nodes in murine inflammatory arthritis. *PLoS One* **8**, e73766 (2013).
817 79. H. M. Kenney *et al.*, A high-throughput semi-automated bone segmentation workflow for
818 murine hindpaw micro-CT datasets. *Bone Rep* **16**, 101167 (2022).
819 80. M. Vrecl *et al.*, Effect of the ostreolysin A/pleurotolysin B pore-forming complex on intracellular
820 Ca2+ activity in the vascular smooth muscle cell line A10. *Toxicol In Vitro* **29**, 2015-2021 (2015).

821

822

823 **Figure Legends**

824 **Figure 1. Generation and validation of CreER^{T2} transgenic mice with tamoxifen-inducible**
825 **gene expression in PLV adventitial cells. a** Schematic illustration of the P2A-CreER^{T2}
826 targeting vectors that were used to generate the knock-in transgenic mice as described in
827 Methods. **b** Schematic illustration of tdT reporter studies performed to assess tissue-specific
828 tamoxifen-inducible gene expression in the CreER^{T2} knock-in transgenic mice in which founder
829 lines were crossed with B6.Cg-*Gt(ROSA)26Sor*$^{tm9(CAG\text{-}tdTomato)Hze}$/J (Ai9) mice to generate *Efhd1*,
830 *Myoc* and *Pla1a* CreER$^{+/-}$ x Ai9$^{+/-}$ test mice and single-transgenic Ai9$^{+/-}$ littermate controls. **c** An
831 illustration of the tamoxifen dosing regimen (daily intraperitoneal injections on postnatal days
832 10–13) to the 3 lines of male and female mice ($n \geq 5$) is presented with the standard time of
833 sacrifice at postnatal day 21. **d** WMIFM was performed on PLV immunostained with FITC-
834 conjugated anti-αSMA antibodies from the indicated tamoxifen-treated mice. Representative 4x
835 images of tdT^{+} cells (red) surrounding αSMA^{+} (green) in Efhd1CreER$^{+/-}$ x Ai9$^{+/-}$ and
836 MyocCreER$^{+/-}$ x Ai9$^{+/-}$ mice after tamoxifen induction, but not in CreER negative controls.

837

838 **Figure 2. Efhd1-CreER^{T2} targets two populations of PLV adventitial cells that are adjacent**
839 **to mast cells. a** WMIFM of PLV from tamoxifen-treated Efhd1-CreER$^{+/-}$x Ai9$^{+/-}$ mice was
840 performed as described in Figure 1 and a 4x image is show with 10x images of the boxed ROIs
841 highlighting **b** a tdT^{+} telocyte-like cell with its telopode (arrow) aligned along the surface of the
842 PLV, and **c** a network of tdT^{+} telocyte-like cells in the adipose tissue adjacent to the vessels. **d**
843 Evan's blue dye was injected into the footpad of a tamoxifen-treated *Efhd1*-CreER^{T2} x Ai9
844 mouse to image the PLVs for dissection, and the tissue was immunostained with fluorescent
845 antibodies against CD34 and aSMA, and counterstained with DAPI. **e-g** Low power and high-

846 power confocal microscopy images of the ROI (box) confirm immunostaining of the mast cells
847 elaborating the tdT^+ network along the PLV (green). **h** Eight fluorescent low power images of an
848 immunostained full-length PLV with associated tissues were stitched together to imaging
849 telocyte networks that extends from capillaries in the ankle synovium to cLV near the knee. The
850 box indicates the ROI shown in **e-g**.

851

852 **Figure 3. TEM and WMIFM imaging of pre-PLV mast cells physically integrated into**
853 **telocyte arrays. a** TEM was performed on the PLVs described in Fig. 2 and a representative
854 x1000 image is shown highlighting the endothelium (yellow) and smooth muscle (green) layers,
855 cells with telocyte ultrastructural morphology (red), and a mast cell (magenta). A high power
856 x5,000 image of the boxed region is shown highlighting the telocyte-like cell (red arrow)
857 physically integrated into a mast cell (purple arrow), and remnants of a network of telocyte-like
858 cells (yellow arrow). **b** PLV with tdT^+ telocyte-like cells (red) were labelled with fluorescent
859 antibodies against αSMA (green) and mast cell tryptase (MCT; magenta) for WMIF confocal
860 microscopy, and a representative 3D rendering is shown. Note several mast cells are tethered to
861 the tdT^+ telocyte-like cell network (**Supplemental Video 1**). The magnified image of the boxed
862 ROI illustrates the physical integration, as the distance between the mast cell and tdT^+ telocyte-
863 like cell is less than 500nm.

864

865 **Figure 4. Transcriptome confirmation of PLV-associated telocytes and the loss of PLV**
866 **extracellular matrix (ECM) and telocytes in TNF-tg mice. a** Published scRNAseq data on
867 PLV-associated cells from mice(*32*) were reanalyzed to identify the $Pdgfr\alpha^+/Cd34^+$ population

868 known to contain telocytes and adventitial fibroblasts(*9*), and a color-coated UMAP of these
869 populations associated with WT PLV is presented to demonstrate their proportions. **b** UMAPs of
870 known marker genes selectively expressed in one cell type or both telocytes and fibroblasts are
871 shown to further define these populations. **c** Monocle-3 analysis of the scRNAseq data was
872 performed to generate UMAPs with pseudotime predictions (heat maps), hypothesized telocyte
873 differentiation into fibroblasts (lines within the UMAPs), and the 52.3% decrease in the
874 telocytes:fibroblasts ratio in TNF-tg mice relative to their WT littermates ($p>10\text{-}15$ via Fisher's
875 test). **d** Representative x5000 SEM image of a PLV from a WT mouse with intact ECM
876 structure, associated mast cell (magenta arrow), and an apparent telocyte cell body (red arrow)
877 embedded in the ECM. Representative x5000 SEM images of PLVs from TNF-tg mice, **e** one
878 with partial ECM loss and exposed LMCs (green arrows), and **f** one with extensive ECM and
879 LMC loss. **g** Immunohistochemistry was performed on knees sections from WT, TNF-tg mice
880 receiving Placebo or Anti-TNF treatment from a prior study(*26*), and representative fluorescent
881 microscopy images are shown with quantification of the $CD31^{-}/CD34^{+}$ cells as a percentage of
882 synoviocytes ($n=3$; $p<0.001$ t-test).

883

884 **Figure 5. Similarities between synovial and PLV-associated tdT^{+} cells with a telocyte**
885 **phenotype and their distinctions from fibroblasts. a** Experimental workflow showing
886 tamoxifen treatment of Efhd1-$CreER^{+/-}$x $Ai9^{+/-}$ mice followed by tissue harvest, cell isolation,
887 and subsequent analyses. **b** Flow cytometric analysis of knee and ankle synovial tissues revealing
888 distinct tdT^{high} and tdT^{low} populations (red arrows). **c** UMAPs showing expression of telocyte
889 and fibroblast marker genes in knee synovial cells, matching the expression patterns observed in
890 Figure 3b. **d** Representative immunofluorescence images of knee and ankle sections from

891 tamoxifen-treated Efhd1-CreER$^{+/-}$ x Ai9$^{+/-}$ mice stained for Comp (green) and DAPI (blue),
892 demonstrating distinct spatial localization of telocytes near the meniscus attachment sites while
893 fibroblasts (Comp^{+}) occupy peripheral regions. Images at 1x magnification with 5x
894 magnification of boxed region are shown with parallel H&E bright field images.

895

896 **Figure 6. In vivo depletion of telocytes decreases lymphatic function**. **a** Schematic illustration
897 of the tamoxifen-induced telocyte deletion model generated by crossing Efhd1- CreER^{T2} mice
898 DTA-floxed mice. The efficiency of in vivo telocyte deletion following tamoxifen treatment was
899 assessed via **b** WMIFM of PLVs and **c** IHC of knee synovium with quantification of the relative
900 telocyte percentage as described in Fig. 3, from the double transgenic mice and their DTA$^{f/-}$
901 littermates. **d** Histomorphometric quantification of relative telocyte percentage (n=3; $p < 0.5$* or
902 0.001*** vs. Placebo treated TNF-tg via t-test). **e** Lymphatic clearance in tamoxifen-treated
903 Efhd1- CreER$^{+/-}$ x DTA$^{f/-}$ mice and their DTA$^{f/-}$ littermate controls was assessed via NIR-ICG
904 imaging, and representative IVIS images of the ICG injected into the footpads at the time of
905 injection (Baseline) and 6hrs later are shown with the heatmap of the signal intensity and %
906 lymphatic clearance for each foot. **f** Data on the % lymphatic clearance of the cohort before and
907 after tamoxifen injection are presented for each mouse with the mean for the group ($n \geq 6$; $p<0.05$
908 via t-test). Similar results were obtained in experiments with Myoc- CreER$^{+/-}$ x DTA$^{f/-}$ mice (data
909 not shown).

910

911 **Figure 7. Telocyte depletion increases severity and duration of synovial inflammation from**
912 **zymosan induced arthritis (ZIA)**. **a** Experimental design and workflow in which 8-week-old

913 female WT and Efhd1-CreER$^{+/-}$ x DTA$^{f/-}$ mice received tamoxifen treatment to introduce telocyte
914 depletion in DTA double-transgenics. Knee injections of zymosan or PBS were given at 10-
915 weeks of age followed by knee ultrasound pre-knee injection and on days- 2, 7, and 14 post-knee
916 injection. Mice were euthanized on day-15 and knee joints were harvested for histology. **b**
917 Representative day-14 knee ultrasound images of the synovial volume between the femur (f) and
918 tibia (t) that were quantified longitudinally (**c** AUC values with mean +/- SD; $p<0.01$, ANOVA)
919 and prior to sacrifice on day-14 time (**d**; **$p \leq 0.01$ via ANOVA). **e** Representative H&E-stained
920 joint histology obtained at 10x with magnified regions of interest (box) highlighting non-
921 resorbed cortical bone surfaces in PBS WT (white arrows) vs. resorbed cortical bone surface in
922 all other groups (yellow arrows), and the ZIA pannus tissue (#). **f** Quantification of the synovial
923 area is reported as the percentage of ROI, as described in Methods. Data are presented with the
924 mean +/- SD (**$p<0.01$via ANOVA). Similar results were obtained in experiments with Myoc-
925 CreER$^{+/-}$ x DTA$^{f/-}$ mice (data not shown). **g** 3D renderings of the distal femur micro-CT scans,
926 with quantification of the focal erosions (**h;** *$p \leq 0.05$ via ANOVA). Data are presented for each
927 femur with mean +/- SD.

928

929 **Fig. 8 Telocytes exhibit greater sensitivity to osmotic pressure changes and are less invasive**
930 **than fibroblasts. a** Schematic illustration of ex vivo culture of PLVs from tamoxifen treated
931 Myoc-CreER$^{+/-}$x Ai9$^{+/-}$ and Efhd1-CreER$^{+/-}$x Ai9$^{+/-}$ mice, which produce ~1:1 cocultures of tdT^{+}
932 telocytes and tdT^{-} fibroblasts. For osmotic shock study the cells were preloaded with Hoechst,
933 Ca^{++}, and Fluo-4, prior to osmotic shock with various concentrations of sucrose (data not shown)
934 and analyzed via real-time fluorescent microscopy. **b** Representative 10x fluorescent images of a
935 coculture post-sucrose stimulation are shown to illustrate Ca^{++} responsiveness seen as green

936 fluorescence (center). The ROI (boxes) are magnified to illustrate four cell types: non-responsive
937 telocytes (red), responsive telocytes (yellow), non-responsive fibroblasts (blue), and responsive
938 fibroblasts (green) with (top) and without (bottom) the superimposed tdT channel. The response
939 to 100 μM (424.5 mOsm) sucrose was quantified as the % Fluo-4 positive telocytes or
940 fibroblasts, and the data are plotted with the mean +/- SD (** $p<0.01$, t-test, each data point
941 represents the mean value of 4 images from a single chamber from an independent experiment).
942 **c** Matrigel invasion assays were performed with transwell insert containing cells in serum-free
943 media that invaded towards 10% FBS containing media -/+ 5ng/ml TGF-beta in the bottom
944 chamber for 24hr. The culture was Hoechst-stained prior to fluorescent confocal microscopy, and
945 representative 3D reconstructed images are shown with top and side views illustrating the red
946 telocytes on top of the blue nuclei within the fibroblasts. The migration depth of each nucleus in
947 the Matrigel was calculated and presented in the histograms, which are representative of three
948 independent experiments.

949

950 **Figure 9. PLV-associated telocytes differentiate into fibroblasts on stiff ECM.** Primary
951 cultures of the FACS purified tdT^+ cells described in Fig. 4 were cultured on collagen-coated
952 CytoSoft® Imaging 24-well plates with varying stiffness levels: 0.2 kPa (soft), 8 kPa
953 (intermediate), and 64 kPa (stiff). After 24hrs of culture the cells were harvested for bulk RNA
954 sequencing and gene expression analyses. **a** Normalized expression of telocyte (*Efhd1* and *Myoc*)
955 and myofibroblast (*Acta2* and *Tagln*) maker genes are graphed as a function of the ECM
956 stiffness. **b** The quantified change in the indicated telocyte, myofibroblast, and fibroblast marker
957 gene expression is presented with changes as indicated by the key. Also presented are the in

958 significantly expressed *TIMP*, *Collagen* and *MMP* genes. All indicated changes are significant
959 ($p>0.05$).

960

961 **Figure 10. Proposed telocyte networks within the synovial lymphatic system of the lower**
962 **limb and their regulation of joint homeostasis and lymphatic function. a** Schematic model of
963 telocyte regulation of PLV stiffness. Telocytes with telopods integrated along PLV monitor
964 stiffness and remodel the ECM. When the PLV is too flaccid the telocytes produce myocilin to
965 crosslink the collagen and fibronectin in the ECM (black arrow). When the PLV becomes too
966 rigid from ECM accumulation, telocytes release matrix metalloproteases (MMPs) and
967 downregulate tissue inhibitors of MMPs (TIMPs) to degrade the ECM (white arrow). In the
968 absence of telocytes in TNF-tg mice, chronic inflammation perpetuates MMP breakdown of the
969 ECM and dysfunction of flaccid PLV (red arrow). **b** Schematic model of telocyte network
970 regulation of PLV contraction in the mouse lower limb. Telocytes in the synovium monitor
971 extracellular osmotic pressure in joint fluid and are activated upon sensing an excessive
972 threshold (left). Upon activation, an intercellular signal is transmitted through the network of
973 telopode-to-telopode connected telocytes and is ultimately delivered to mast cells adjacent to the
974 joint-draining cLV. This signal triggers mast cell degranulation and release of vasoconstricting
975 factors (e.g. histamine) that initiate LMC contractions in the resting PLV. Subsequent diastole
976 assisted by ECM tensile force generates vacuum suction to fill the PLV with lymph from the
977 joint (middle), and the intraluminal shear force triggers intrinsic PLV contractions by LMCs,
978 which then clears the excess interstitial fluid in the joint returning it to normal osmotic pressure
979 (right).

980

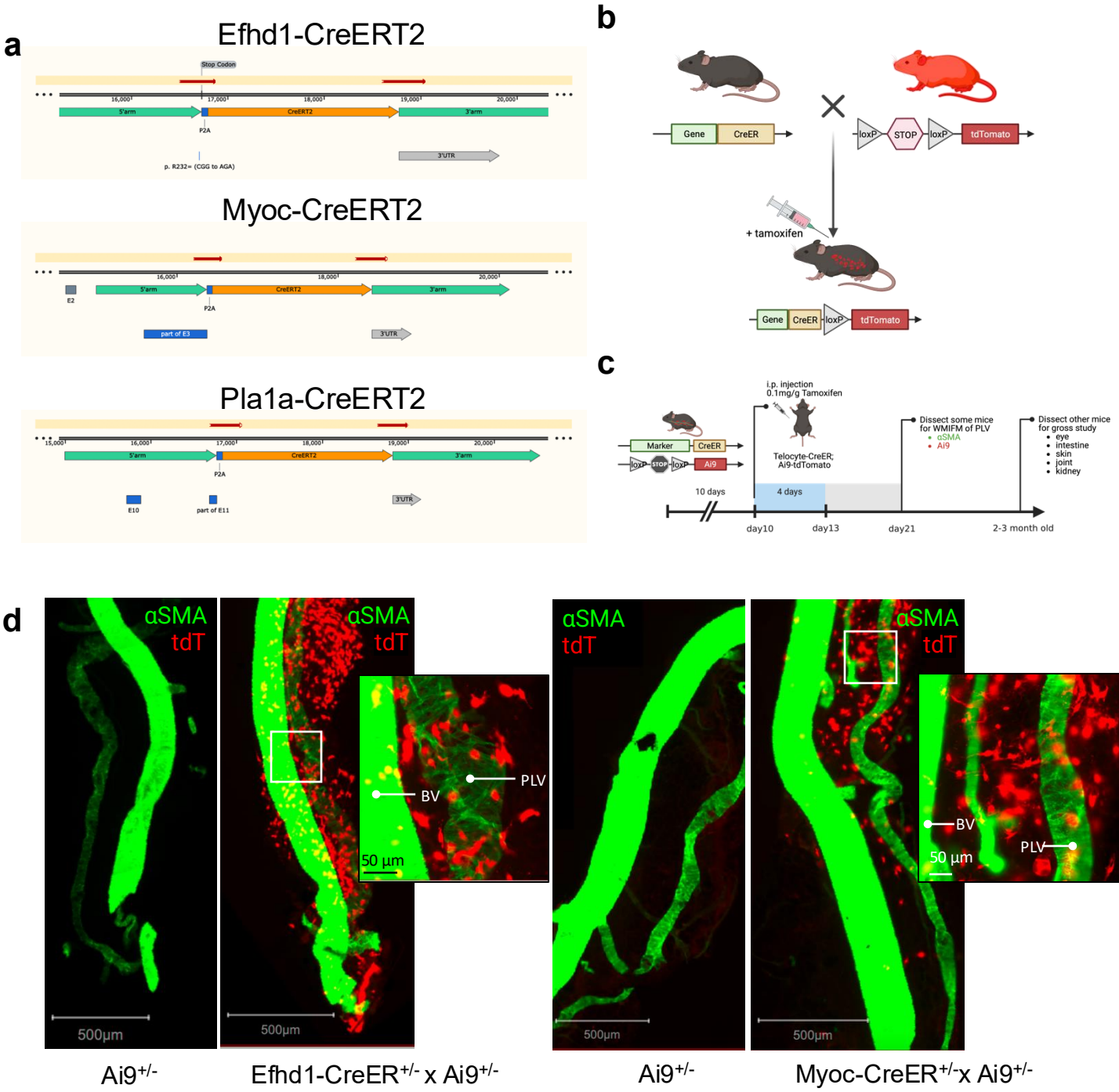

Fig. 1 Generation and validation of CreERT2 transgenic mice with tamoxifen-inducible gene expression in PLV adventitial cells. a Schematic illustration of the P2A-CreERT2 targeting vectors that were used to generate the knock-in transgenic mice as described in Methods. **b** Schematic illustration of tdT reporter studies performed to assess tissue-specific tamoxifen-inducible gene expression in the CreERT2 knock-in transgenic mice in which founder lines were crossed with B6.Cg-*Gt(ROSA)26Sor*$^{tm9(CAG\text{-}tdTomato)Hze}$/J (Ai9) mice to generate *Efhd1*, *Myoc* and *Pla1a* CreERT2$^{+/-}$ x Ai9$^{+/-}$ test mice and single-transgenic Ai9$^{+/-}$ littermate controls. **c** An illustration of the tamoxifen dosing regimen (daily intraperitoneal injections on postnatal days 10–13) to the 3 lines of male and female mice ($n \geq 5$) is presented with the standard time of sacrifice at postnatal day 21. **d** WMIFM was performed on PLV immunostained with FITC-conjugated anti-αSMA antibodies from the indicated tamoxifen-treated mice. Representative 4x images of tdT^{+} cells (red) surrounding αSMA^{+} (green) in Efhd1CreER$^{+/-}$ x Ai9$^{+/-}$ and MyocCreER$^{+/-}$ x Ai9$^{+/-}$ mice after tamoxifen induction, but not in CreER negative controls.

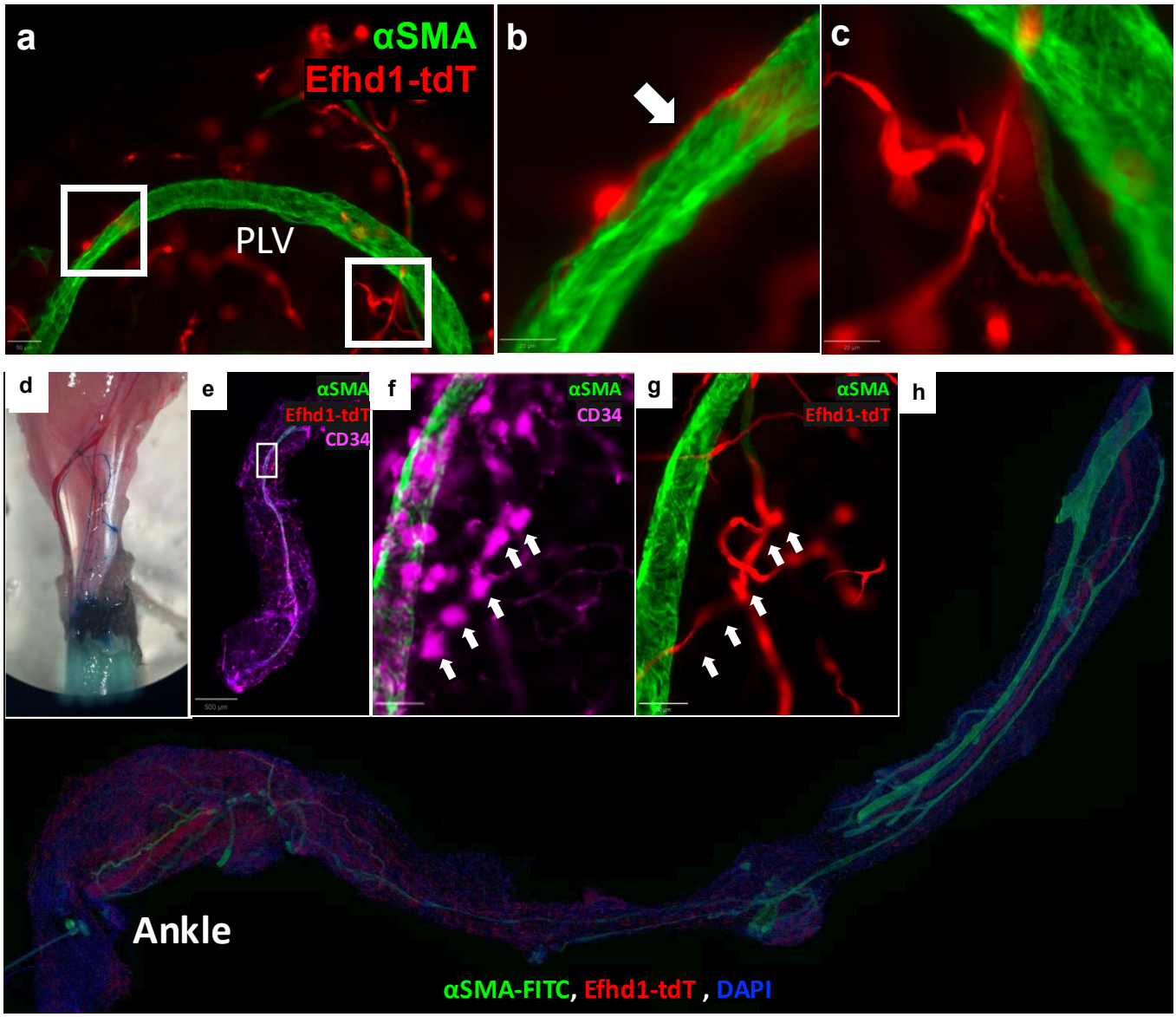

Fig. 2 Efhd1-CreERT2 targets two populations of PLV adventitial cells that are adjacent to mast cells. a WMIFM of PLV from tamoxifen-treated Efhd1-CreER$^{+/-}$x Ai9$^{+/-}$ mice was performed as described in Figure 1 and a 4x image is show with 10x images of the boxed ROIs highlighting **b** a tdT^{+} telocyte-like cell with its telopode (arrow) aligned along the surface of the PLV, and **c** a network of tdT^{+} telocyte-like cells in the adipose tissue adjacent to the vessels. **d** Evan's blue dye was injected into the footpad of a tamoxifen-treated *Efhd1*-CreERT2 x Ai9 mouse to image the PLVs for dissection, and the tissue was immunostained with fluorescent antibodies against CD34 and αSMA, and counterstained with DAPI. **e-g** Low power and high-power confocal microscopy images of the ROI (box) confirm immunostaining of the mast cells elaborating the tdT^{+} network along the PLV (green). **h** Eight fluorescent low power images of an immunostained full-length PLV with associated tissues were stitched together to imaging telocyte networks that extends from capillaries in the ankle synovium to cLV near the knee.

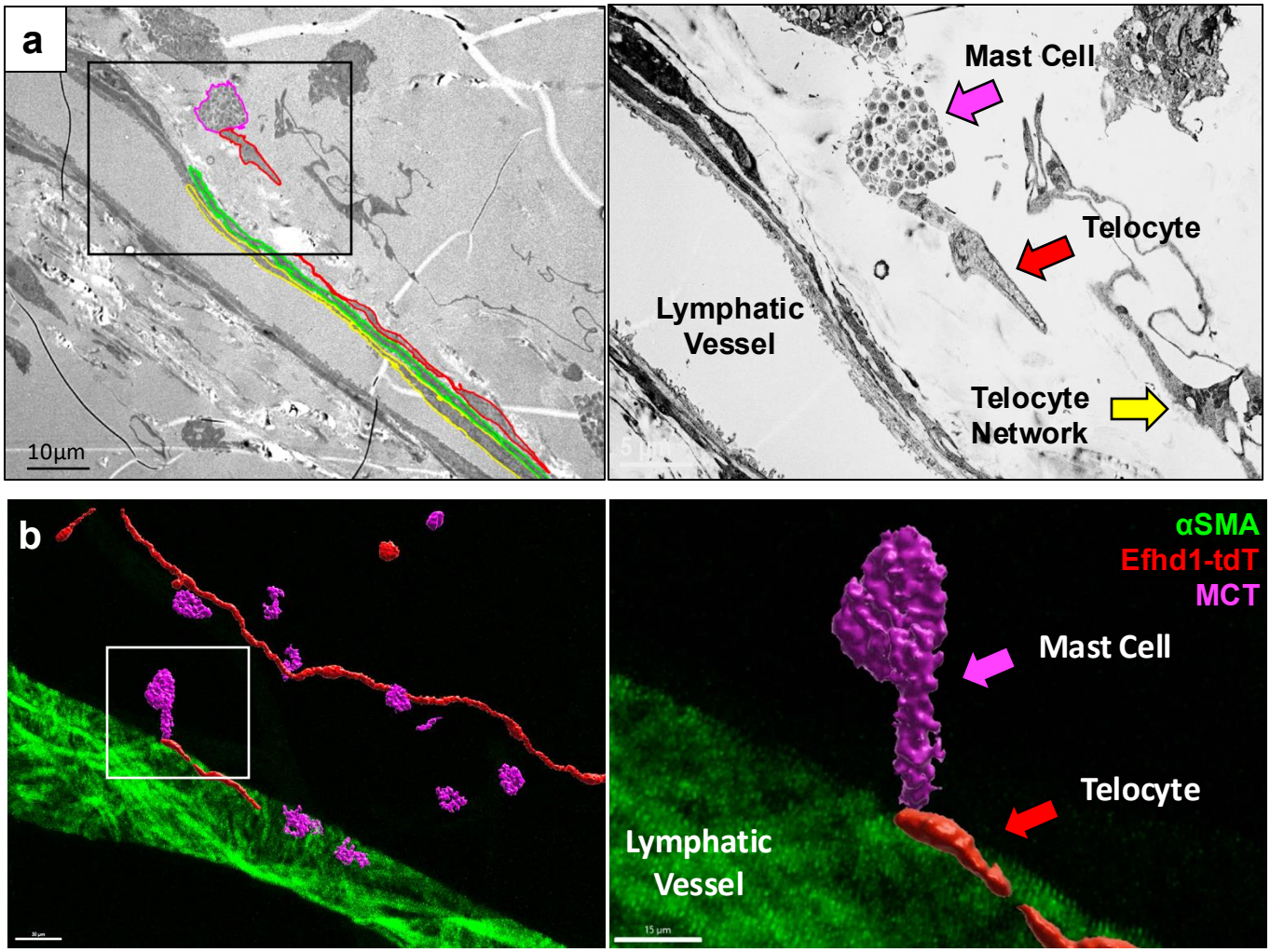

Fig. 3 TEM and WMIFM imaging of pre-PLV mast cells physically integrated into telocyte arrays. a TEM was performed on the PLVs described in Fig. 2 and a representative x1000 image is shown highlighting the endothelium (yellow) and smooth muscle (green) layers, cells with telocyte ultrastructural morphology (red), and a mast cell (magenta). A high power x5,000 image of the boxed region is shown highlighting the telocyte-like cell (red arrow) physically integrated into a mast cell (purple arrow), and remnants of a network of telocyte-like cells (yellow arrow). **b** PLV with tdT^+ telocyte-like cells (red) were labelled with fluorescent antibodies against αSMA (green) and mast cell tryptase (MCT; magenta) for WMIF confocal microscopy, and a representative 3D rendering is shown. Note several mast cells are tethered to the tdT^+ telocyte-like cell network (**Supplemental Video 1**). The magnified image of the boxed ROI illustrates the physical integration, as the distance between the mast cell and tdT^+ telocyte-like cell is less than 500nm.

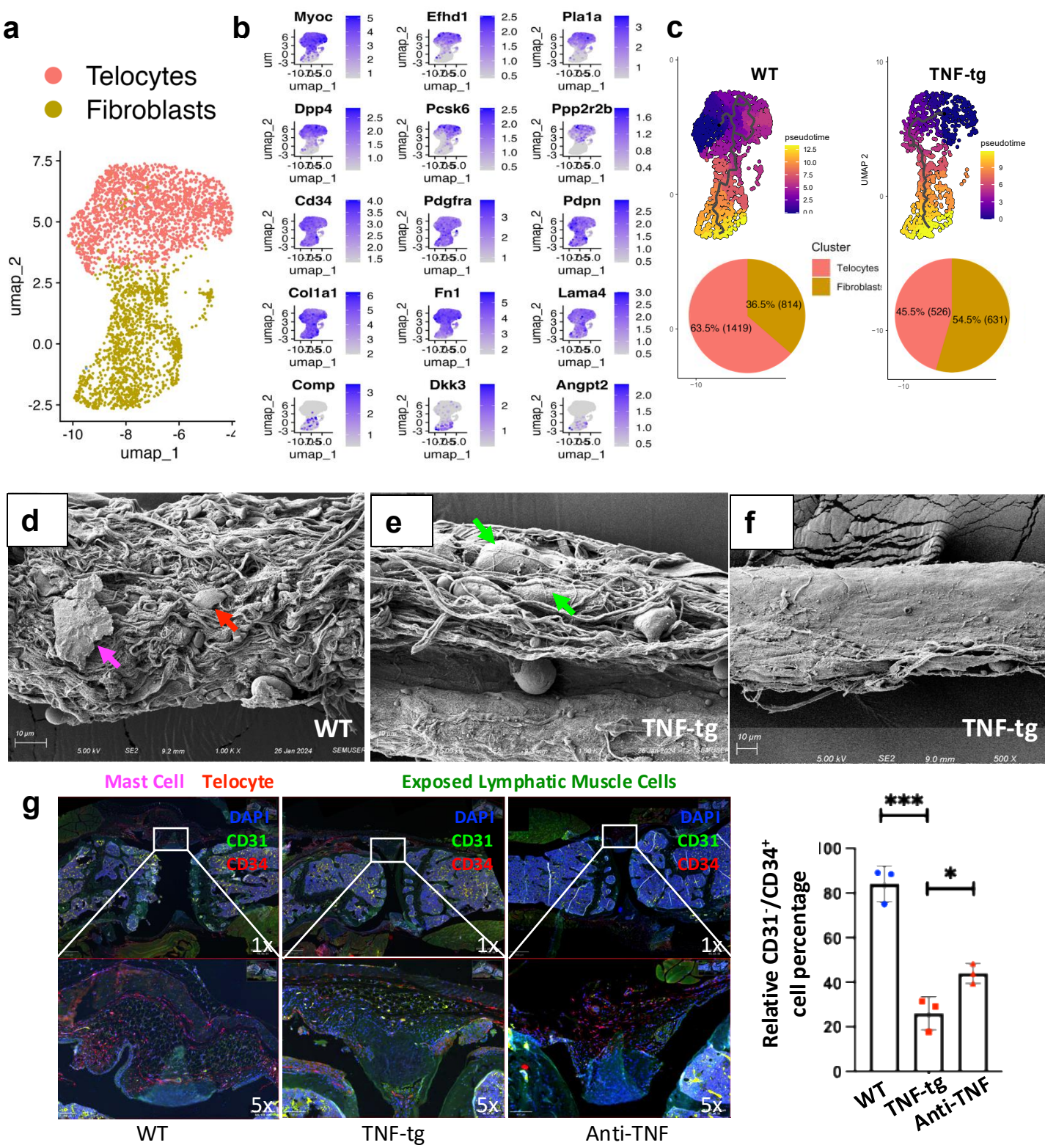

Fig. 4 Transcriptome confirmation of PLV-associated telocytes and the loss of PLV extracellular matrix (ECM) and telocytes in TNF-tg mice. a Published scRNAseq data on PLV-associated cells from mice[47] were reanalyzed to identify the Pdgfrα^{+}/Cd34^{+} population known to contain telocytes and adventitial fibroblasts[13], and a color-coated UMAP of these populations associated with WT PLV is presented to demonstrate their proportions. **b** UMAPs of known marker genes selectively expressed in one cell type or both telocytes and fibroblasts are shown to further define these populations. **c** Monocle-3 analysis of the scRNAseq data was performed to generate UMAPs with pseudotime predictions (heat maps), hypothesized telocyte differentiation into fibroblasts (lines within the UMAPs), and the 52.3% decrease in the telocytes:fibroblasts ratio in TNF-tg mice relative to their WT littermates (p>10-15 via Fisher's test). **d** Representative x5000 SEM image of a PLV from a WT mouse with intact ECM structure, associated mast cell (magenta arrow), and an apparent telocyte cell body (red arrow) embedded in the ECM. Representative x5000 SEM images of PLVs from TNF-tg mice, **e** one with partial ECM loss and exposed LMCs (green arrows), and **f** one with extensive ECM and LMC loss. **g** Immunohistochemistry was performed on knees sections from WT, TNF-tg mice receiving Placebo or Anti-TNF treatment from a prior study[26], and representative fluorescent microscopy images are shown with quantification of the CD31^{-}/CD34^{+} cells as a percentage of synoviocytes (n=3; p<0.001 t-test).

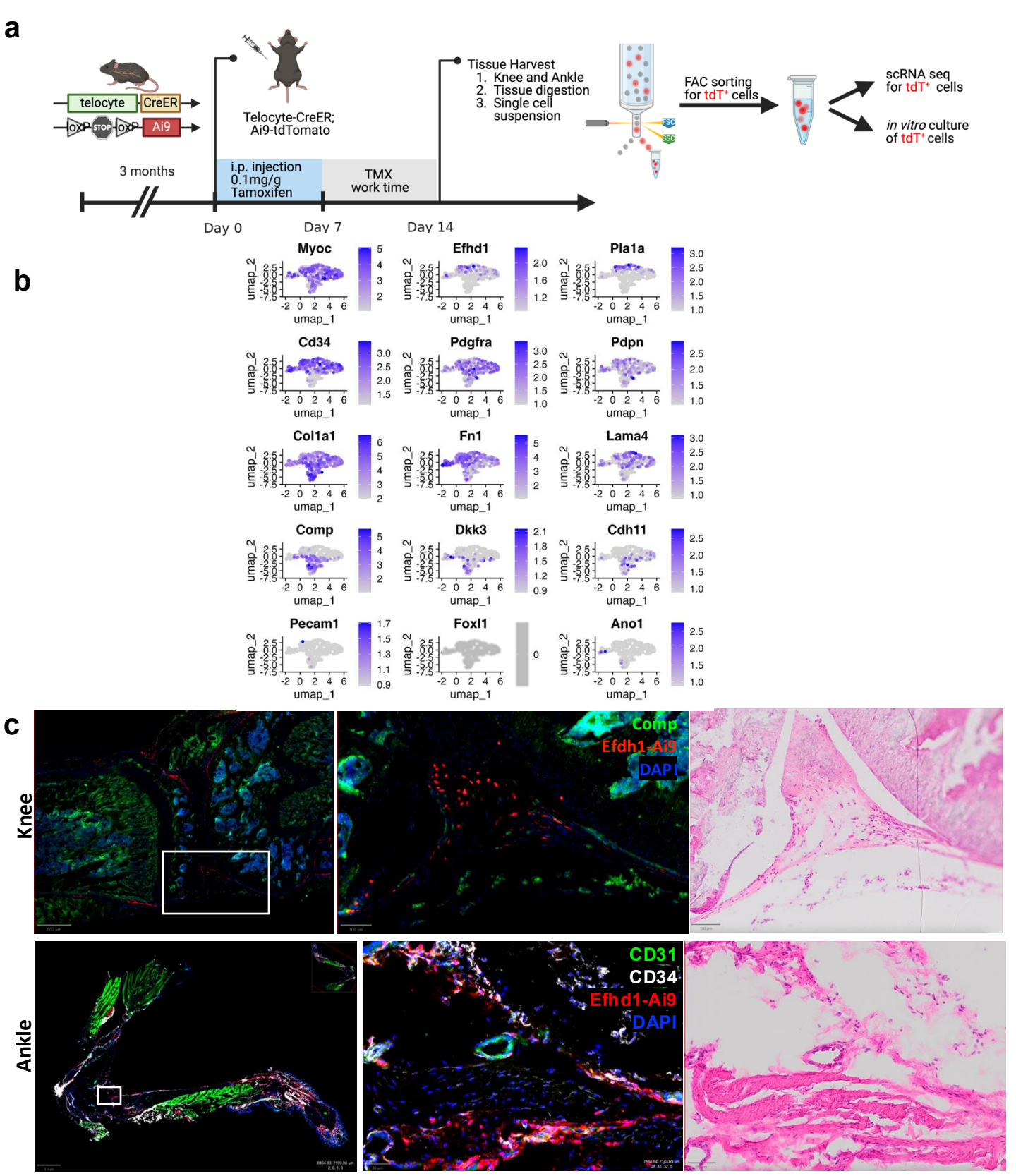

Fig. 5 Similarities between synovial and PLV-associated tdT^{+} cells with a telocyte phenotype and their distinctions from fibroblasts. a Experimental workflow showing tamoxifen treatment of Efhd1-CreER$^{+/-}$x Ai9$^{+/-}$ mice followed by tissue harvest, cell isolation, and subsequent analyses. **b** Flow cytometric analysis of knee and ankle synovial tissues revealing distinct tdT^{high} and tdT^{low} populations (red arrows). **c** UMAPs showing expression of telocyte and fibroblast marker genes in knee synovial cells, matching the expression patterns observed in Figure 3b. **d** Representative immunofluorescence images of knee and ankle sections from tamoxifen-treated Efhd1-CreER$^{+/-}$ x Ai9$^{+/-}$ mice stained for Comp (green) and DAPI (blue), demonstrating distinct spatial localization of telocytes near the meniscus attachment sites while fibroblasts (Comp^{+}) occupy peripheral regions. Images at 1x magnification with 5x magnification of boxed region are shown with parallel H&E bright field images.

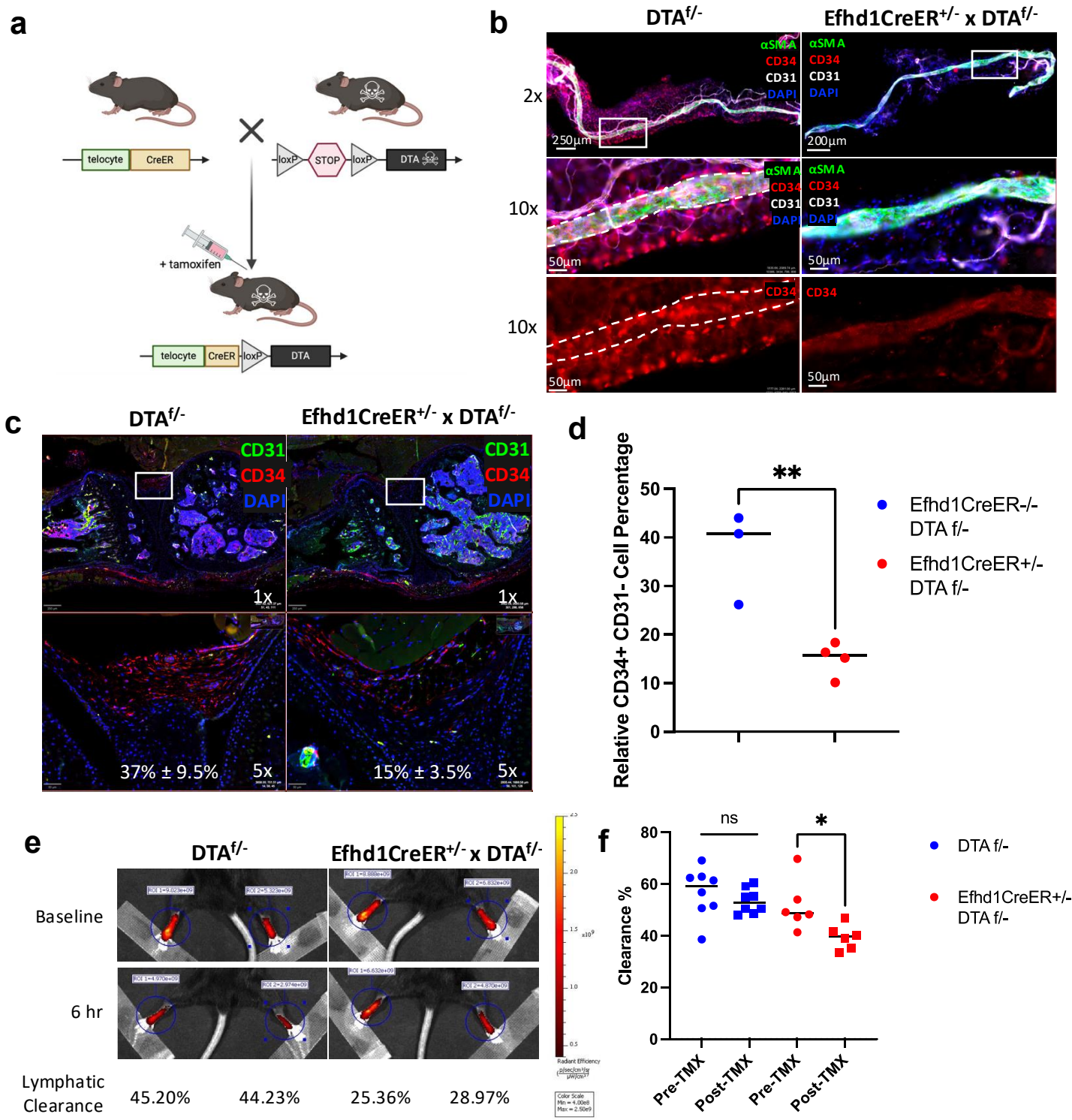

Fig. 6 In vivo depletion of telocytes decreases lymphatic function. **a** Schematic illustration of the tamoxifen-induced telocyte deletion model generated by crossing Efhd1-CreERT2 mice DTA-floxed mice. The efficiency of in vivo telocyte deletion following tamoxifen treatment was assessed via **b** WMIFM of PLVs and **c** IHC of knee synovium with quantification of the relative telocyte percentage as described in Fig. 3, from the double transgenic mice and their DTA$^{f/-}$ littermates. **d** Histomorphometric quantification of relative telocyte percentage (n=3; $p < 0.5$* or 0.001*** vs. Placebo treated TNF-tg via t-test). **e** Lymphatic clearance in tamoxifen-treated Efhd1-CreERT2$^{+/-}$ x DTA$^{f/-}$ mice and their DTA$^{f/-}$ littermate controls was assessed via NIR-ICG imaging, and representative IVIS images of the ICG injected into the footpads at the time of injection (Baseline) and 6hrs later are shown with the heatmap of the signal intensity and % lymphatic clearance for each foot. **f** Data on the % lymphatic clearance of the cohort before and after tamoxifen injection are presented for each mouse with the mean for the group ($n \geq 6$; $p<0.05$ via t-test). Similar results were obtained in experiments with Myoc-CreERT2$^{+/-}$ x DTA$^{f/-}$ mice (data not shown).

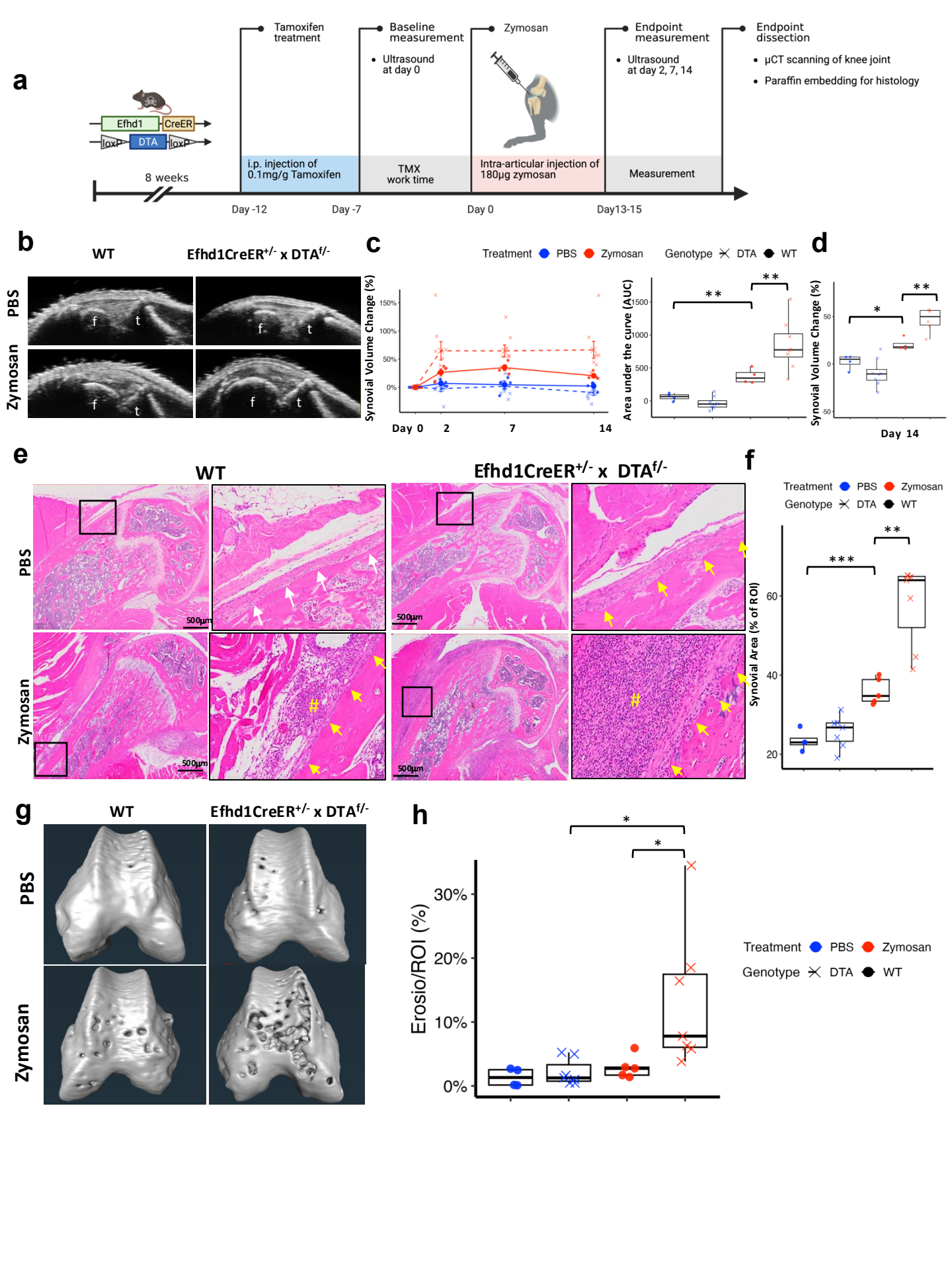
a
Tamoxifen treatment
Baseline measurement
Ultrasound at day 0
Zymosan
Endpoint measurement
Ultrasound at day 2, 7, 14
Endpoint dissection
μCT scanning of knee joint
Paraffin embedding for histology
Efhd1
CreER
loxP
DTA
loxP
8 weeks
i.p. injection of 0.1mg/g Tamoxifen
TMX work time
Intra-articular injection of 180μg zymosan
Measurement
Day -12
Day -7
Day 0
Day13-15
b
WT
Efhd1CreER+/- x DTAf/-
PBS
Zymosan
f
t
c
Treatment PBS Zymosan
Genotype DTA WT
Synovial Volume Change (%)
Day 0
2
7
14
Area under the curve (AUC)
d
Synovial Volume Change (%)
Day 14
e
WT
Efhd1CreER+/- x DTAf/-
PBS
Zymosan
500μm
f
Treatment PBS Zymosan
Genotype DTA WT
Synovial Area (% of ROI)
g
WT
Efhd1CreER+/- x DTAf/-
PBS
Zymosan
h
Erosio/ROI (%)
Treatment PBS Zymosan
Genotype DTA WT

Fig. 7 Telocyte depletion increases severity and duration of synovial inflammation from zymosan induced arthritis (ZIA). **a** Experimental design and workflow in which 8-week-old female WT and Efhd1-CreERT2$^{+/-}$ x DTA$^{f/-}$ mice received tamoxifen treatment to introduce telocyte depletion in DTA double-transgenics. Knee injections of zymosan or PBS were given at 10-weeks of age followed by knee ultrasound pre-knee injection and on days- 2, 7, and 14 post-knee injection. Mice were euthanized on day-15 and knee joints were harvested for histology. **b** Representative day-14 knee ultrasound images of the synovial volume between the femur (f) and tibia (t) that were quantified longitudinally (**c** AUC values with mean +/- SD; $p<0.01$, ANOVA) and prior to sacrifice on day-14 time (**d**; **$p \leq 0.01$ via ANOVA). **e** Representative H&E-stained joint histology obtained at 10x with magnified regions of interest (box) highlighting non-resorbed cortical bone surfaces in PBS WT (white arrows) vs. resorbed cortical bone surface in all other groups (yellow arrows), and the ZIA pannus tissue (#). **f** Quantification of the synovial area is reported as the percentage of ROI, as described in Methods. Data are presented with the mean +/- SD (**$p<0.01$via ANOVA). Similar results were obtained in experiments with Myoc-CreERT2$^{+/-}$ x DTA$^{f/-}$ mice (data not shown). **g** 3D renderings of the distal femur micro-CT scans, with quantification of the focal erosions(**h;** *$p \leq 0.05$ via ANOVA). Data are presented for each femur with mean +/- SD.

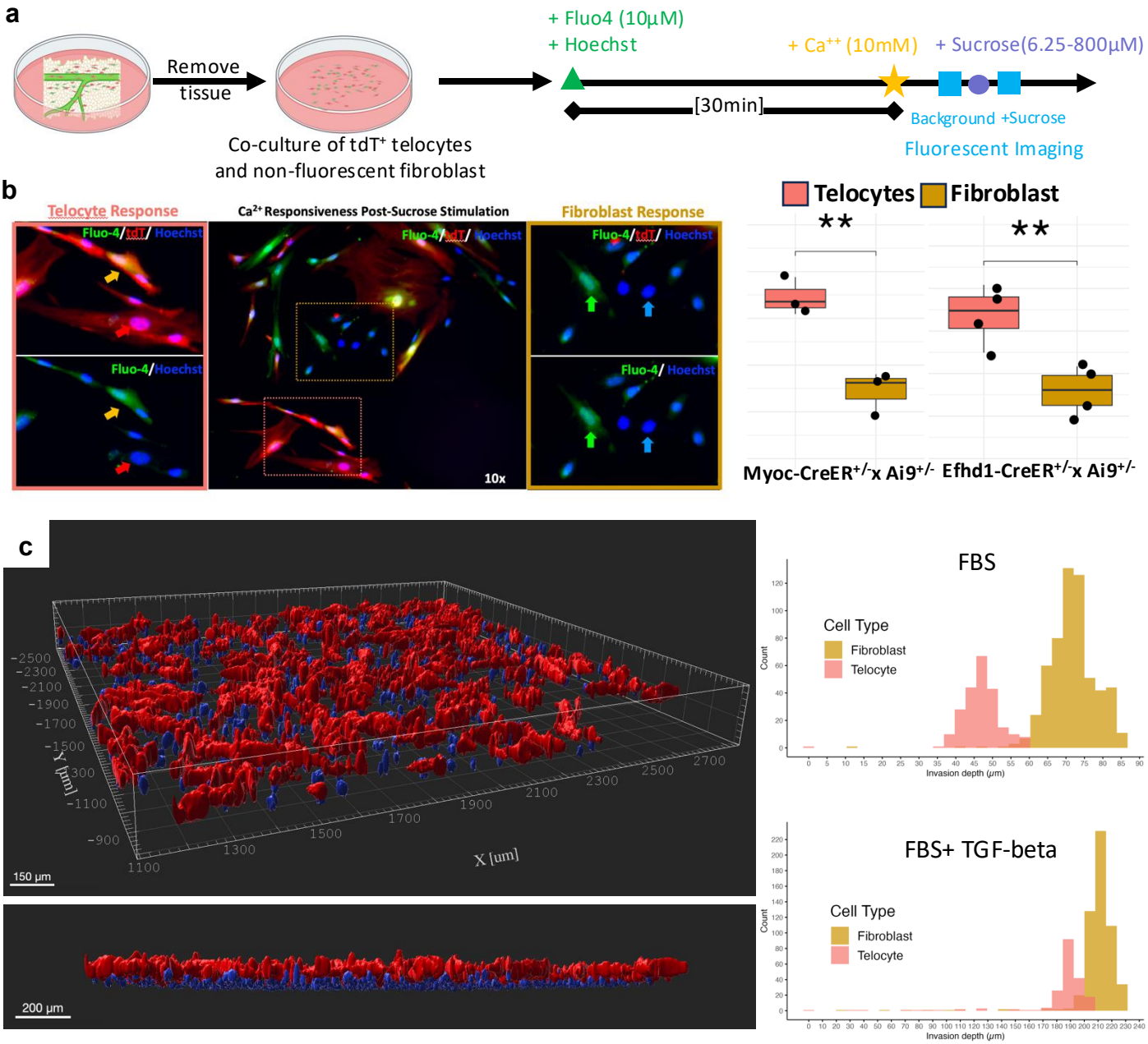

Fig. 8 Telocytes exhibit greater sensitivity to osmotic pressure changes and are less invasive than fibroblasts. **a** Schematic illustration of ex vivo culture of PLVs from tamoxifen treated Myoc-CreER$^{+/-}$x Ai9$^{+/-}$ and Efhd1-CreER$^{+/-}$x Ai9$^{+/-}$ mice, which produce ~1:1 cocultures of tdT^{+} telocytes and tdT^{-} fibroblasts. For osmotic shock study the cells were preloaded with Hoechst, Ca^{++}, and Fluo-4, prior to osmotic shock with various concentrations of sucrose (data not shown), and analyzed via real-time fluorescent microscopy. **b** Representative 10x fluorescent images of a coculture post-sucrose stimulation are shown to illustrate Ca^{++} responsiveness seen as green fluorescence (center). The ROI(boxes) are magnified to illustrate four cell types: non-responsive telocytes (red), responsive telocytes (yellow), non-responsive fibroblasts (blue), and responsive fibroblasts (green) with (top) and without (bottom) the superimposed tdT channel. The response to 100 µM (424.5 mOsm) sucrose was quantified as the % Fluo-4 positive telocytes or fibroblasts, and the data are plotted with the mean +/- SD (** $p<0.01$, t-test, each data point represents the mean value of 4 images from a single chamber from an independent experiment). **c** Matrigel invasion assays were performed with transwell insert containing cells in serum-free media that invaded towards 10% FBS containing media -/+ 5ng/ml TGF-beta in the bottom chamber for 24hr. The culture was Hoechst-stained prior to fluorescent confocal microscopy, and representative 3D reconstructed images are shown with top and side views illustrating the red telocytes on top of the blue nuclei within the fibroblasts. The migration depth of each nuclei in the Matrigel was calculated and presented in the histograms, which are representative of three independent experiments.

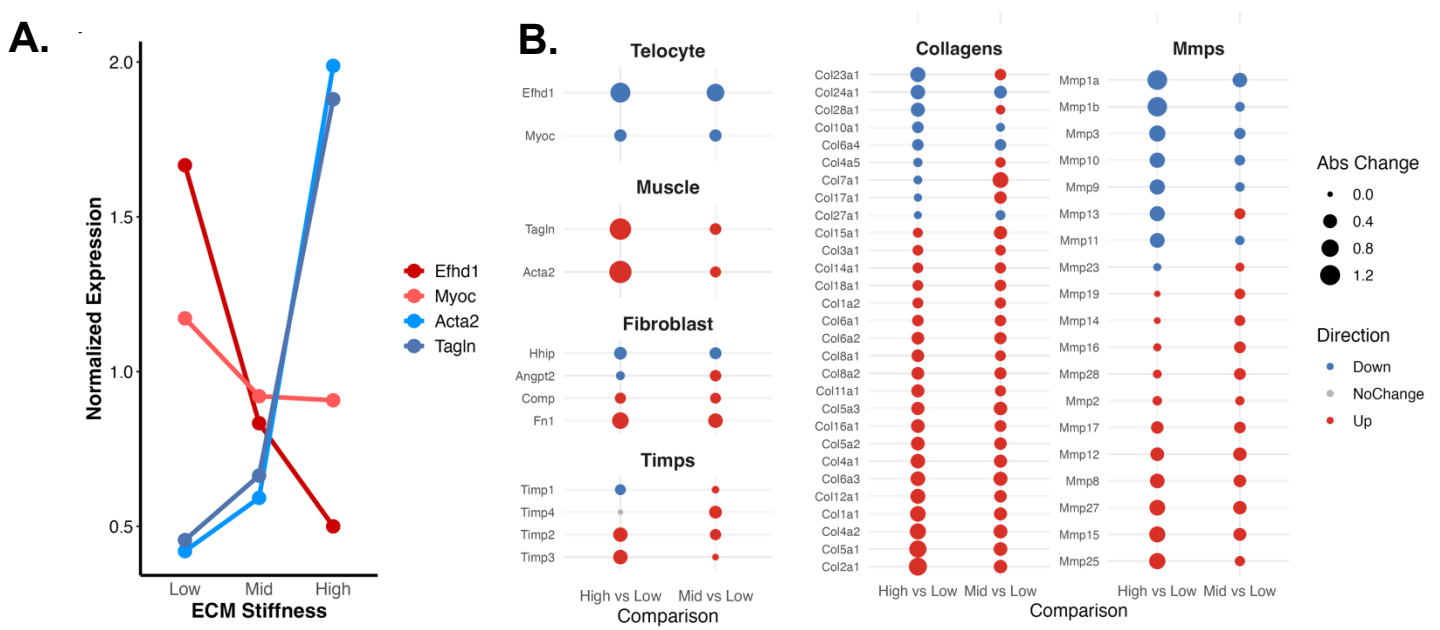

Fig. 9 PLV-associated telocytes differentiate into fibroblasts on stiff ECM. Primary cultures of the FACS purified tdT^{+} cells described in Fig. 4 were cultured on collagen-coated CytoSoft® Imaging 24-well plates with varying stiffness levels: 0.2 kPa (soft), 8 kPa (intermediate), and 64 kPa (stiff). After 24hrs of culture the cells were harvested for bulk RNA sequencing and gene expression analyses. **a** Normalized expression of telocyte (*Efhd1* and *Myoc*) and myofibroblast (*Acta2* and *Tagln*) maker genes are graphed as a function of the ECM stiffness. **b** The quantified change in the indicated telocyte, myofibroblast, and fibroblast marker gene expression is presented with changes as indicated by the key. Also presented are the in significantly expressed *TIMP*, *Collagen* and *MMP* genes. All indicated changes are significant ($p>0.05$).

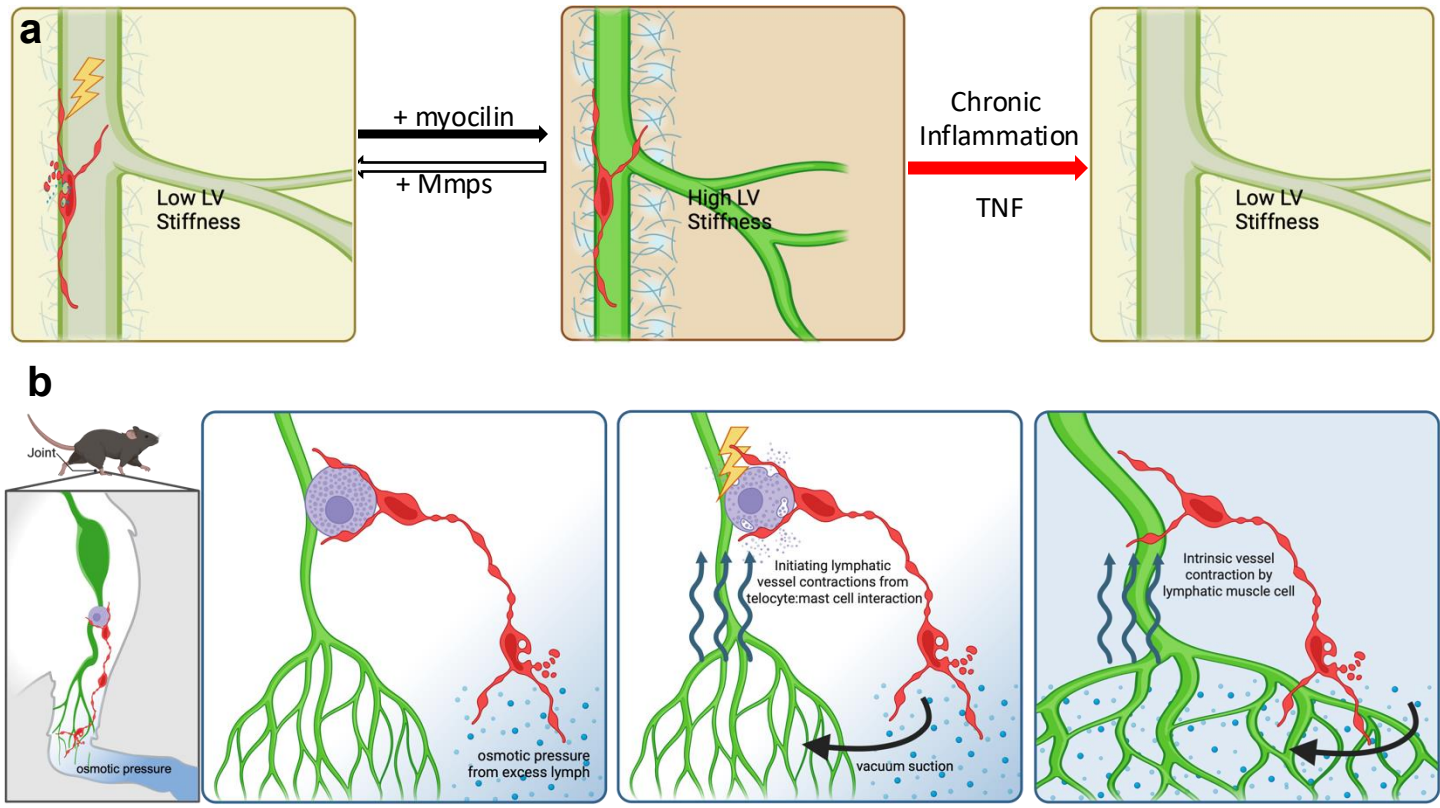

Fig. 10 Proposed telocyte networks within the synovial lymphatic system of the lower limb and their regulation of joint homeostasis and lymphatic function. **a** Schematic model of telocyte regulation of PLV stiffness. Telocytes with telopods integrated along PLV monitor stiffness and remodel the ECM. When the PLV is too flaccid the telocytes produce myocilin to crosslink the collagen and fibronectin in the ECM (black arrow). When the PLV becomes too rigid from ECM accumulation, telocytes release matrix metalloproteases (MMPs) and downregulate tissue inhibitors of MMPs (TIMPs) to degrade the ECM (white arrow). In the absence of telocytes in TNF-tg mice, chronic inflammation perpetuates MMP breakdown of the ECM and dysfunction of flaccid PLV (red arrow). **b** Schematic model of telocyte network regulation of PLV contraction in the mouse lower limb. Telocytes in the synovium monitor extracellular osmotic pressure in joint fluid and are activated upon sensing an excessive threshold (left). Upon activation, an intercellular signal is transmitted through the network of telopod-to-telopod connected telocytes and is ultimately delivered to mast cells adjacent to the joint-draining cLV. This signal triggers mast cell degranulation and release of vasoconstricting factors (e.g. histamine) that initiate LMC contractions in the resting PLV. Subsequent diastole assisted by ECM tensile force generates vacuum suction to fill the PLV with lymph from the joint (middle), and the intraluminal shear force triggers intrinsic PLV contractions by LMCs, which then clears the excess interstitial fluid in the joint returning it to normal osmotic pressure (right).